Catalytic Reaction Mechanism of Glyoxalase II

A Quantum Mechanics/Molecular Mechanics Study

Shirazi, Javad; Jafari, Sonia; Ryde, Ulf; Irani, Mehdi

Published in:
Journal of Physical Chemistry B

DOI:
10.1021/acs.jpcb.3c01495

2023

Document Version:
Peer reviewed version (aka post-print)

Catalytic Reaction Mechanism of Glyoxalase II, a Quantum Mechanics/Molecular Mechanics Study

Javad Shirazi,[1] Sonia Jafari, [1] Ulf Ryde, [2] Mehdi Irani [1]*

[1] Department of Chemistry, University of Kurdistan, P.O. Box 66175-416, Sanandaj, Iran

[2] Department of Theoretical Chemistry, Lund University, P.O. Box 124, SE-221 00 Lund, Sweden

Correspondence to Mehdi Irani, E-mail: m.irani@uok.ac.ir,

Tel: +98 – 9128018046

2024-04-28

Abstract

Methylglyoxal (MG) is a reactive and toxic compound produced in carbohydrate, lipid, and amino acid metabolism. The glyoxalase system is the main detoxifying route for MG and consists of two enzymes, glyoxalase I (GlxI) and glyoxalase II (GlxII). GlxI catalyzes the formation of *S*-D-lactoylglutathione from hemithioacetal, and GlxII converts this intermediate to D-lactate. A relationship between the glyoxalase system and some diseases like diabetes has been shown, and inhibiting enzymes of this system may be an effective means of controlling certain diseases. A detailed understanding of the reaction mechanism of an enzyme is essential to the rational design of competitive inhibitors. In this work, we use quantum mechanics/molecular mechanics (QM/MM) calculations and energy refinement utilizing the big-QM and QM/MM thermodynamic cycle perturbation methods to propose a mechanism for the GlxII reaction that starts with a nucleophilic attack of the bridging OH^- group on the substrate. The coordination of the substrate to the Zn ions places its electrophilic center close to the hydroxide group, enabling the reaction to proceed. Our estimated reaction energies are in excellent agreement with experimental data, thus demonstrating the reliability of our approach and the proposed mechanism. Additionally, we examined alternative protonation states of Asp-29, 58, 134 and the bridging hydroxide ion in the catalytic process. However, these give less favorable reactions, a poorer reproduction of the crystal-structure geometry of the active site, and higher root-mean-squared deviations of the active-site residues in molecular dynamics simulations.

Keywords: glyoxalase II, methylglyoxal, mechanism, biocatalysis, QM/MM, protonation states

1. Introduction

Methylglyoxal (MG) is a reactive and toxic compound that is produced in carbohydrate, lipid, and amino acid metabolism. [1–3] In addition, MG is produced nonenzymatically from glyceraldehyde 3-phosphate[4] and aminoacetone.[5,6] The ubiquitous glyoxalase system is the main detoxifying route for MG.[7] In addition to the glyoxalase route, other enzymes also participate in the detoxification of MG.[8] In particular, aldose reductase functions as a ketone reductase in the presence of glutathione (H-SG), reducing MG to lactaldehyde[9] (cf. Scheme 1 for structures).

The glyoxalase system was discovered in 1913,[10,11] and consists of two enzymes, glyoxalase I (EC 4.4.1.5, lactoylglutathione lyase; GlxI) and glyoxalase II (hydroxyacylglutathione hydrolase, EC 3.1.2.6; GlxII). The reaction catalyzed by the system is shown in Scheme 1. It converts the *R*- and *S*-hemithioacetals (HTA) of MG and H-SG into D-lactate.[12,13] GlxI catalyzes the formation of *S*-D-lactoylglutathione (*S*-LG) from HTA and GlxII converts this intermediate to D-lactic acid (due to its low pK_a value of 3.9, D-lactate is the stable form of D-lactic acid). D-Lactate can then be converted into pyruvate, the main substrate used to generate ATP through aerobic respiration.[14] In general, GlxII hydrolyzes various α-hydroxythioesters to the corresponding non-cytotoxic α-hydroxycarboxylic acids, regenerating H-SG.[15] Because of the ability of *S*-LG to inhibit DNA synthesis, *S*-LG is also cytotoxic.[16,17] The relationship between the glyoxalase system and diabetes has been studied because an accumulation of MG in diabetes patients can lead to pathophysiological complications.[18,19] It has also been targeted in developing anti-protozoal and anti-tumor drugs.[20]

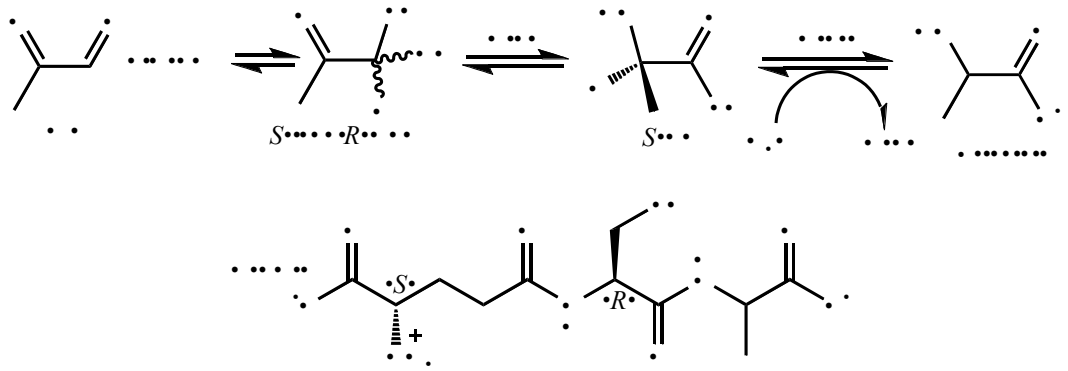

Scheme 1. The glyoxalase system is composed of GlxI and GlxII and catalyzes the conversion of MG into D-lactate via *S*-LG, using H-SG as a cofactor.

GlxII from various sources, including mammals,[21,22] plants,[23] yeast,[24,25] and protozoan parasites,[13,26,27] has an isoelectric point generally above pH 7. GlxII is primarily found in the matrix of the mitochondria.[28] Purified GlxII is unstable but can be stabilized with glycerol.[15] This enzyme is inhibited weakly by H-SG[29] and strongly by HTA, the substrate of GlxI.[30,31] A variety of derivatives of H-SG also inhibit the enzyme.[32,33] The strongest inhibitors are *S*-substituted-carbobenzoxy H-SG derivatives.[34] One report indicates that GlxII may also be essential in regulating spermatogenesis.[35] It has recently been shown that GlxII is associated with the proapoptotic Bax protein in non-small-cell lung cancer and that this complex plays an influential non-enzymatic role in regulating apoptosis.[36] In

contrast to GlxI, GlxII activity is found both in cytosol and mitochondria.[37–40] There are two GlxII isozymes in *Plasmodium falciparum*, one of which is housed within the apicoplast.[41] Researchers have recently demonstrated intense staining in the nuclei of human prostate cancer cells, but not of their normal counterparts, using a polyclonal antibody against GlxII.[42] Inhibiting GlxII may therefore be an effective means of controlling certain diseases. A detailed understanding of the reaction mechanism of an enzyme is essential to the rational design of competitive inhibitors. Our aim in this research is to understand how GlxII catalyzes its reaction.

GlxII is a binuclear metalloenzyme with Zn(II) as the most frequently observed metal ion. However, cytosolic and mitochondrial GlxII from *Arabidopsis thaliana* contains varying ratios of Zn(II), Fe(II), and Mn(II).[15,43] Some GlxII enzymes are also activated by Ni(II) and Co(II).[44,45] Human GlxII has also been shown to contain a mixed binuclear center with Zn(II) and Fe(II), although the mononuclear Zn(II) reconstituted enzyme is also active.[44] The coordination sphere of the two metal ions in GlxII varies slightly based on the type of ligand in the active site.[13,22,28,46] In all cases, seven protein residues directly interact with the two metal ions.[13,22,28,46] In human GlxII, a water molecule is also involved in binding the two metal ions, most likely as a hydroxide ion.[22] The active site of human GlxII and its coordinating ligands are shown in Figure 1.

This enzyme shows a broad specificity for thiol esters of H-SG, and *S*-LG is generally its preferred substrate.[47] However, GlxII from some species prefers other substrates. For example, *S*-D-lactoyltrypanothione is the preferred substrate of *Leishmania infantum* GlxII. The fact that thiol esters such as *S*-LG possess labile α-hydrogens suggests that GlxII may use a carbanion mechanism, i.e., the α-hydrogen is removed before glutathione is eliminated to produce a ketene intermediate.[15] However, NMR studies showed that hydrolysis of *S*-α-deuteriomandeloylglutathione by GlxII does not result in the loss of deuterium, suggesting that a carbanion mechanism is not involved.[33]

In recent years, the reaction mechanisms of several binuclear zinc enzymes have been investigated. The mechanism typically begin with a nucleophilic attack on the substrate by a bridging hydroxide ion. After that, the reaction proceeds with one or two proton transfer steps. A brief overview of studies of the reaction mechanism of other binuclear zinc enzymes is given in the Supporting Information.[48–54]

For GlxII, Vander Jagt (VJ) proposed in 1993 that an active-site histidine residue attacks *S*-LG and forms a covalent enzyme–substrate (E-S) complex, leading to glutathione liberation[15] (cf. Scheme 2). On the other hand, Cameron et al. postulated a reaction mechanism for GlxII based on the position of *S*-(N-hydroxy-N-bromophenylcarbamoyl) glutathione (HBPC–GSH) in the active site.[22] Based on their proposed mechanism, the reaction is initiated by a nucleophilic attack on the carbonyl carbon of the substrate by the bridging hydroxide oxygen. This attack produces a negatively charged tetrahedral intermediate. According to them, the bond between the carbonyl carbon and sulfur atoms of the substrate must be broken to complete the reaction, H-SG must be protonated, and the products must

diffuse away from the active site to be replaced by water molecules. However, they were not sure how this process occurs.

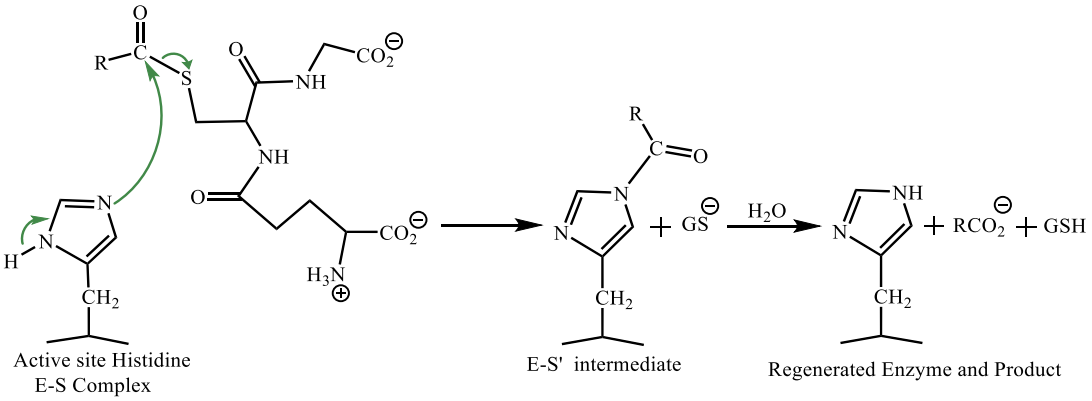

Scheme 2. A schematic of the proposed mechanism by VJ.[15]

Based on mutational, kinetic, and crystallographic data, Makaroff et al.[55] proposed an overall reaction mechanism for the cytoplasmic form of GlxII from *Arabidopsis* (cf. Scheme 3). They demonstrated that the enzyme contains an iron–zinc binuclear metal center that is essential for its function. Their mechanism involves the nucleophilic attack of the bridging hydroxide oxygen on the carbonyl carbon of the substrate, resulting in the formation of a tetrahedral transition state. In the following step, a ligand exchange occurs at one of the metal centers, and a water molecule replaces D-lactic acid. The water molecule protonates the GS^- moiety of *S*-LG, generates H-SG as a leaving group, and regenerates the active site.

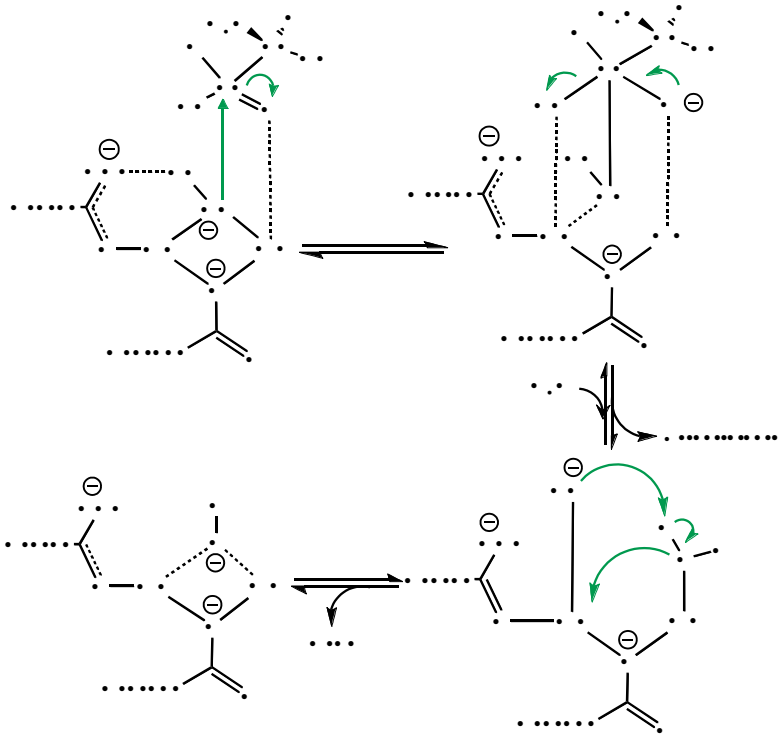

Scheme 3. Makaroff's mechanism for the GlxII reaction.[55]

A three-step mechanism was proposed by Himo et al.,[56] shown in Scheme 4. They used density functional theory (DFT) methods and a small QM-cluster model of the GlxII active site manually cut

out from the crystal structure (PDB code 1QH5).[22] Their model contained the zinc ions and their first-shell ligands, His-54, His-56, His-110, Asp-58, His-59, His-173, and the bridging Asp-134 and hydroxide (μ-OH^-; 78 atoms in total). The ligands in their model were truncated, such that histidines were represented by imidazole and aspartates by acetate. They utilized a thioester derived from lactic acid and methylthiol as a model of *S*-LG. In their proposed mechanism, the first step is the nucleophilic attack of the bridging hydroxide oxygen (Oμ) on the carbonyl carbon (Cs) of the substrate (atom names are indicated in Scheme 4). In the following step, the hydroxide proton, Hμ, is transferred to OD1 of Asp-58. Next, the Cs–S bond is cleaved, forming a thiolate (GS^-) and lactate coordinating to Zn1 and Zn2, respectively.

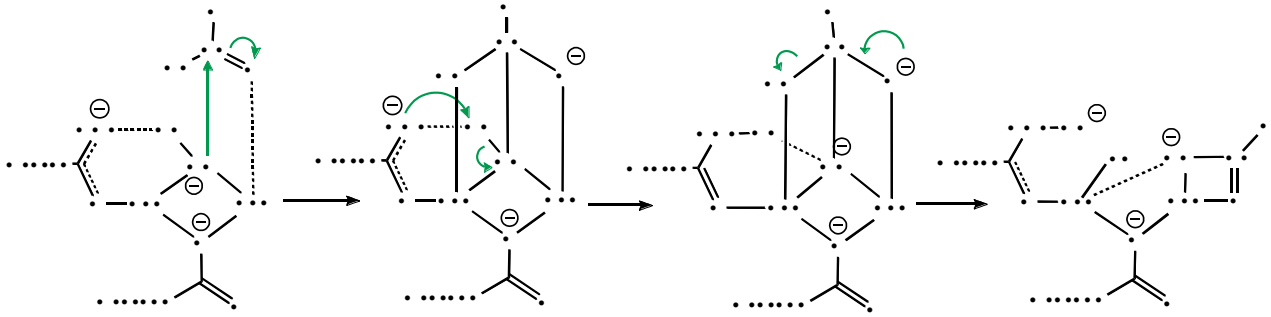

Scheme 4. Himo's mechanism for the GlxII reaction.[56]

The reaction mechanism of GlxI has been thoroughly investigated using QM/MM.[57–59] In this work, we examine the catalytic reaction of GlxII, using this method. In contrast to previous work that used a QM cluster approach,[56] our QM/MM method explicitly includes the entire protein in the calculations (cf. section 2.2). We also used MD simulations to identify the proper protonation states of some active site residues. We identify possible mechanisms for this reaction and compare them with those previously presented.

2. Methods

2.1 Protein Setup

All calculations were based on the 1.45 Å resolution crystal structure of human GlxII (PDB code 1QH5),[22] composed of two subunits (A and B). Each chain has 260 amino acids and one active-site pocket. The active site of chain A contains two Zn(II) ions and one H-SG molecule. The active-site cavity of chain B also has two Zn(II) ions but one *S*-(N-hydroxy-N-bromophenyl carbamoyl) glutathione molecule (GBP), which mimics the substrate (*S*-LG). For the QM/MM calculations (described in section 2.3), we removed the complete chain A and built the substrate by modifying the GBP molecule (replacing (4-bromophenyl)-hydroxycarbamoyl with (2*R*)-2-hydroxypropanoyl). However, in the MD simulations (described in section 2.2), we kept both chains and all hetero groups (i.e., chain A contained H-SG, and chain B contained a GBP molecule).

Protonation states of all residues were determined by studying the possible formation of ionic

pairs, hydrogen-bond patterns, and solvent accessibility. The assigned protonation states were also checked by PROPKA (protein pK_a) calculations.[60–62] Based on this, all Arg, Lys, and Asp residues were assumed to be charged. However, we conducted more detailed analyses of the protonation states of the active-site aspartate residues (Asp-29, 58, and 134) using MD simulations (cf. section 3.2). Glu-218 was assumed to be protonated (because it is buried with no nearby compensating charged groups), but all the other Glu residues were negatively charged. All Cys residues were assumed to be protonated. A thorough manual inspection of all His residues gave the following protonation assignment: His-54, 55, 59, 110, 114, and 173 were protonated on the ND1 atom, His-43, 87, 91, 185, and 235 were protonated on both the ND1 and NE2 atoms (and therefore positively charged), whereas His-56 was modeled with a proton on the NE2 atom.

2.2 MD simulations

All MD simulations were performed using the GPU-accelerated *pmemd* module[63–65] of AMBER 20.[66] The protein was modeled by the Amber ff14SB[67] force field, and the general Amber force field (GAFF)[68] was used to for the ligands. To calculate GAFF parameters of hetero-molecules, they were optimized at the B3LYP/6-31G(d)[69–73] level of theory, and electrostatic potentials were calculated at the Hartree−Fock/6-31G(d) level of theory with points sampled according to the Merz−Kollman scheme.[74] They were calculated by Gaussian 16 program package.[75] Atomic charges were then fitted to these potentials using the restrained electrostatic potential procedure,[76] as implemented in the *antechamber* program,[76] which also assigned GAFF atom types to the molecules. The topology and parameter files for H-SG and GBP are given in the Supporting Information.

Metal sites were treated with a nonbonded model with restraints between metals and their ligands. This is necessary to keep the structure of the metal cluster intact.[77] The distances between the metals and their ligands were restrained to those found in the crystal structure (averaged over subunits) and force constants derived from QM frequency calculations. Partial atomic charges of metal centers were calculated by QM methods. In these QM calculations, we used the optimized structure of the model shown in Figure S9 in the Supporting Information (the Zn ions and their coordination ligands; Zn1(OH^-)(Asp-58)(His-59)(Asp-134)(His173) and Zn2(OH^-)(His-54)(His-56)(His-110)(Asp-134)). The calculations were performed at the TPSS/def2-SV(P) level of theory,[78,79] using the Turbomole software (version 7.1)[80] and sped up by the resolution-of-identity approximation[81,82] and empirical dispersion corrections were included with the DFT-D3 approach[83] and Becke−Johnson damping,[84] as implemented in Turbomole. The force constants were calculated by the method of Seminario using the Hess2FF software.[85,86] The restraints and charges are given in Tables S1 and S2 in the Supporting Information.

The setup of the MD simulations is similar to that in our recent works.[58,87] First, the protonated protein was immersed in a periodic truncated octahedral box of TIP3P water molecules,[88] extending at

least 10 Å from the solute using the *tleap* program in the Amber suite. We also added approximately 96 Cl^- and 110 Na^+ ions (depending on the protonation state of the Asp and Oμ groups) to neutralize the protein and give it an ionic strength of 0.15 M to the systems. These ions were added by replacing random water molecules with the *tleap* program in Amber. The parameters for the ions were obtained from the *frcmod.ionsjc_tip3p* force field.[89] The final system contained ~32 700 atoms. The system was then subjected to 1000 cycles of minimization, restraining heavy atoms toward the starting crystal structure with a force constant of 100 kcal/mol/Å^2. After that, two 20 ps equilibrations (one with constant volume and one with constant pressure) were performed with the same restraints, but the force constant was 50 kcal/mol/Å^2. Next, the system was equilibrated for 1 ns constant pressure without any restraints. Finally, we performed 100 ns simulations at constant pressure and coordinates were sampled every 10 ps.

Mass-weighted root mean squared deviations (RMSDs) were calculated with the AMBER *cpptraj* module,[90] analyzing trajectories with saved coordinates from the production simulations and using the crystal structure as the reference. Reported values are averages over these 10 000 sets of coordinates.

2.3 QM/MM Calculations

To prepare a model for the QM/MM calculations, the protein was solvated in a periodic truncated octahedral box of TIP3P[88] water molecules that extended at least 20 Å from the solute using the *tleap* module of the Amber software suite [91]. The protein and substrate were described with the Amber ff14SB[67] and GAFF[68] force fields, respectively. To equilibrate the system, 1000 cycles of minimization were applied to the hydrogen atoms and 1000 cycles of minimization to both the hydrogen atoms and the added water molecules. After that, a 10 ps constant-volume equilibration with the same constraints was performed. The systems were then equilibrated using the same restraints for 1 ns at constant volume, followed by a 1 ns simulated annealing simulation at constant pressure (the force constant for the restraints was always 1000 kcal/mol/Å^2). The SHAKE method[92] constrained all bonds involving hydrogen atoms (not in the minimizations), allowing for a simulation time step of 2 fs. The temperature was held constant at 300 K with Langevin dynamics[93] and a collision frequency of 2 ps^{-1}. The pressure was maintained at 1 atm using Berendsen's weak coupling isotropic technique[94] with a relaxation time of 1 ps. Particle-mesh Ewald summation[95] with a fourth-order B-spline interpolation and a tolerance of 10^{-5} was used for long-range electrostatics. The cut-off for Lennard-Jones interactions was 8 Å. Finally, equilibrated octahedral system was truncated to a spherical shape with a radius of 35 Å from the geometric center of the prepared system.

Based on this equilibrated structure, we performed QM/MM calculations[96,97] using the ComQum program package.[98,99] In this approach, the protein and solvent are split into two subsystems: System 1 (the QM region) is treated by QM methods and System 2 (the MM region) is represented by MM

methods. The latter system is fixed at the positions of the equilibrated structures.

In the QM part of the QM/MM calculations, system 1 was represented by a wave function, whereas all the other atoms were represented by an array of partial point charges, one for each atom, taken from MM libraries. Thereby, the polarization of the QM system by the surroundings is included in a self-consistent manner. These calculations were performed at the TPSS-D3/def2-SV(P) level of theory,[78,79,81–84] using the Turbomole software[80,100] and were accelerated by the resolution-of-identity approximation.[81,82] The MM part of the QM/MM calculations was performed with the Amber software,[101] using the Amber ff14SB[67] and GAFF[68] force fields for the protein and the substrate, respectively. Water molecules were described by the TIP3P model.[88]

When there is a bond between systems 1 and 2 (a junction), the hydrogen link-atom approach was employed. In this approach, the QM system is capped with hydrogen atoms (hydrogen link atoms, HL), the positions of which are linearly related to the corresponding carbon atoms (carbon link atoms, CL) in the full system.[98,102] All atoms were included in the point-charge model, except the CL atoms.[103] The point charges do not necessarily sum up to an integer, because the Amber force field does not employ charge groups.[101]

The total QM/MM energy in ComQum is calculated by[98,99]

$$E_{\mathrm{QM/MM}} = E^{\mathrm{HL}}_{\mathrm{QM1+ptch2}} + E^{\mathrm{CL}}_{\mathrm{MM12},q_1=0} - E^{\mathrm{HL}}_{\mathrm{MM1},q_1=0} \qquad (1)$$

where $E^{\mathrm{HL}}_{\mathrm{QM1+ptch2}}$ is the QM energy of system 1, truncated by HL atoms and embedded in the set of point charges representing system 2 (but excluding the self-energy of the point charges). $E^{\mathrm{HL}}_{\mathrm{MM1},q_1=0}$ is the MM energy of the QM system, still truncated by HL atoms but without any electrostatic interactions. Finally, $E^{\mathrm{CL}}_{\mathrm{MM12},q_1=0}$ is the classical energy of all atoms in the system with CL atoms and with the charges of the QM system set to zero (to avoid double-counting of the electrostatic interactions). The second and third terms include all bonded and nonbonded terms of the employed MM force field. Using this approach, which is similar to that used in the Oniom method,[104] errors caused by the truncation of the quantum system should partly be canceled out. Thus, ComQum utilizes a subtractive scheme with electrostatic embedding and van der Waals link-atom corrections.[105]

To locate first-order stationary states (reactants, products, and intermediates) we have optimized the structures using the QM/MM method without any restraints. However, to locate transition states (TSs), we scanned reaction coordinates between each stationary point (the distance between two atoms, e.g. O–C, H–O, or H–S) in steps of 0.2 Å (0.1 Å around the maximum point of energy). During the scan, all other degrees of freedom were allowed to relax. The TSs were then approximated as the highest point on the potential energy surface along the reaction coordinates. Due to the size of the QM system, frequency calculations are not possible. However, we have confirmed that once the restraints are released, the TSs return to their respective reactant or product states.

The QM system consisted of the two zinc ions, Asp-58, the active-site histidine ligands (His-54,

56, 59, 110, and 173), the bridging Asp-134 group, the bridging oxygen species, *S*-LG as the substrate, and four water molecules (located at least 6 Å from the Zn ions). Histidines and aspartic acids are included up to the alpha carbon. In the QM/MM calculations, 134–136 and ~19000 atoms were involved in the QM and MM regions, respectively.

To examine the effects of protonation states on the catalytic activity of GlxII, we modified the QM/MM system by switching the protonation state of some groups (Asp-29, 58, and 134 were either charged or protonated, and the bridging oxygen was either an oxide, hydroxide or water molecule). The protonation states of the studied eight systems are described in Table 1 and are denoted PS-I to PS-VIII. The QM system with the first protonation state (PS-I), for which we obtained the reaction paths, is shown in Figure 1 and Scheme 5. The optimized structures of the QM system with the other protonation states are illustrated in Figures S1 to S7 in the Supporting Information.

Table 1. Protonation states of Asp-29, 58, 134, and the bridging oxygen (Oμ) group in QM/MM calculations. The last two columns indicate the total number of atoms and charge of the QM region. ASP is deprotonated, whereas ASH is protonated.

Protonation State	Asp-29	Asp-58	Asp-134	Oμ	**QM atoms**	**QM charge**
PS-I	ASP	ASP	ASP	OH^-	135	0
PS-II	ASH	ASP	ASP	OH^-	135	0
PS-III	ASP	ASH	ASP	OH^-	136	1
PS-IV	ASP	ASP	ASH	OH^-	136	1
PS-V	ASP	ASP	ASP	O^{2-}	134	-1
PS-VI	ASP	ASH	ASP	O^{2-}	135	0
PS-VII	ASP	ASP	ASH	O^{2-}	135	0
PS-VIII	ASP	ASP	ASP	OH_2	136	1

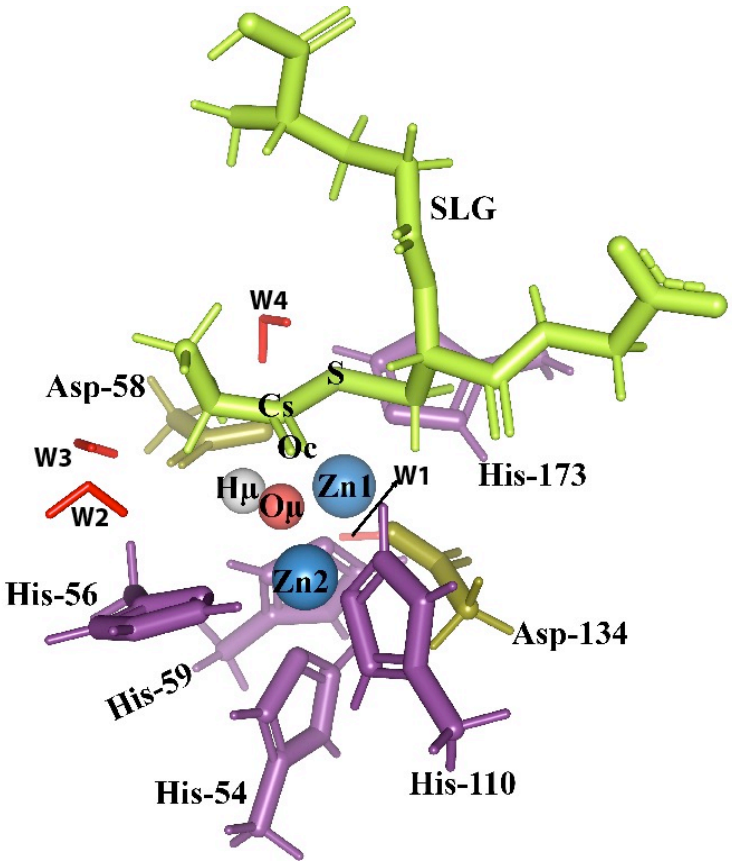

Figure 1. The QM system with PS-I. The Zn and μ-OH ions are depicted by balls and sticks, whereas the other molecules are represented by tubes. The figure is also schematically represented in Scheme 5.

2.4 Big-QM Calculations

Previous studies have shown that QM/MM energies strongly depend on the size of the studied QM system.[103,106] Therefore, we have used the big-QM approach to ensure that the calculated QM/MM energies are converged.[107,108] This approach involves single-point QM/MM calculations on optimized QM/MM structures with a very large QM system, including all atoms within 4.5 Å of the QM system in Figure 1 and all buried charged-residues, and moving junctions at least two residues away from the QM system (resulting 853 and ~19000 atoms in the QM and MM regions, respectively; cf. Figure S8 in the Supporting Information for the QM region).

The QM part of the big-QM calculations was carried out at the TPSS-D3/def2-SV(P) level of theory,[78,79,81–84] as is described in section 2.3, while also utilizing the multipole-accelerated resolution-of-identity J approach (marij keyword).[109] The calculations were carried out with the parallel version of Turbomole.[100] To the big-QM energies, we added the DFT-D3 dispersion correction and a standard MM correction ($E^{\mathrm{CL}}_{\mathrm{MM12},q_{\text{big-QM}}=0} - E^{\mathrm{HL}}_{\mathrm{MM}_{\mathbf{big-QM}},q_{\text{big-QM}}=0}$; cf. Eq1), yielding a standard QM/MM energy but with the big-QM system as the QM region.

These big-QM energies ($E^{\mathrm{SV(P)}}_{\mathbf{big-QM}}$) were improved by extrapolating them to the larger def2-TZVPD basis set, which also includes diffuse functions.[110,111] This was performed by single-point calculations on the original QM region at the TPSS-D3/def2-TZVPD level of theory. Then the big-QM energies were extrapolated to the def2-TZVPD basis set by

$$E_{\mathrm{big-QM}}^{\mathrm{TZVPD}} = E_{\mathrm{big-QM}}^{\mathrm{SV(P)}} + E_{\mathrm{QM1+ptch23}}^{\mathrm{HL,TZVPD}} - E_{\mathrm{QM1+ptch23}}^{\mathrm{HL,SV(P)}} \quad (2)$$

where $E_{\mathrm{big-QM}}^{\mathrm{TZVPD}}$ is the extrapolated big-QM energy, $E_{\mathrm{big-QM}}^{\mathrm{SV(P)}}$ is the normal big-QM energy at the def2-SV(P) level of theory, and, $E_{\mathrm{QM1+ptch23}}^{\mathrm{HL,TZVPD}}$ and $E_{\mathrm{QM1+ptch23}}^{\mathrm{HL,SV(P)}}$ are the QM energy of the normal QM region, truncated by HL atoms and embedded in the set of the point charges, calculated at the TPSS-D3/def2-TZVPD and TPSS-D3/def2-SV(P) levels of theory, respectively.

2.5 QTCP Calculations

We have used QM/MM thermodynamic cycle perturbation (QTCP) to calculate free energy differences between the various states and to improve the quality of the calculated energies.[112] QTCP is a method to calculate free energy differences between the various reaction states with a high-level QM/MM method and uses free-energy perturbation with MD sampling at the MM level.[113–115] These calculations were performed as described before.[115,116] Details of the QTCP calculations are given in the Supporting Information. The big-QM andQTCP calculations are computationally quite demanding and were employed only for the most likely reaction path.

3. Results and discussion

Our study aims to examine the detailed mechanism of the GlxII reaction using the QM/MM method. We test the previously proposed reaction mechanisms, and all reasonable reaction paths, on equal footing. In the following section, we investigate the reaction mechanisms using the QM system with the PS-I protonation state defined in Table 1 and shown in Figure 1, and in the following sections, we will study the effect of altering the protonation states of some active-site groups in the catalytic reaction of GlxII. Reported energies in the following are QM/MM energies, except those in Figure 3, which also include big-QM and QTCP energy corrections.

3.1 Reaction mechanism

The optimized structure of the reactant state (**Re**; i.e. the enzyme–substrate Michaelis complex) is shown in Figure 1, and it is schematically represented in Scheme 5. There are four possible reactions from **Re**, viz., nucleophilic attack of the side chain of His-56 on Cs (the first step in the VJ mechanism; however, VJ did not specify which active-site histidine does this attack; in our optimized **Re** structure, His-56 is the His residue closest to Cs with an ND1–Cs distance of 3.87 Å), nucleophilic attack of Oμ on Cs (the first step of the Himo, Cameron, and Makaroff mechanisms), transfer of Hμ to OD1 of Asp-58, and transfer of Hμ to the sulfur atom of *S*-LG. These reactions are shown by arrows in Scheme 5.

Our calculations showed that the barrier for the nucleophilic attack of the side chain of His-56 on Cs is high (60 kcal/mol). Consequently, we can reject the VJ mechanism. This is expected since the histidine residue is coordinated to one of the Zn ions and cannot dissociate easily. The two last reactions (Hμ to OD1 of Asp-58 and Hμ to S) are not possible because the hydrogen atoms return to the starting point after releasing any bond constraints. However, our results show that the second

reaction (Oμ to Cs) can take place with a barrier and a reaction energy of 7.7 and 6.5 kcal/mol, respectively. The corresponding values in Himo's work are 19.2 and 19.1 kcal/mol. The difference between our calculated barrier and Himo's can be related to differences in the methods, in particular, that we explicitly included the whole protein in our calculations. It is interesting to examine the effect of the Zn ions in this reaction. As is shown in Figure 1 and Scheme 5, the S and Oc atoms of the substrate are weakly interacting with Zn1 and Zn2 in **Re**, respectively, as the sixth ligands in a quasi-octahedral geometry (the S–Zn1 and Oc–Zn2 distances are 3.54 and 2.84 Å). This brings the Cs atom of the substrate close to Oμ, with a distance of 2.61 Å, making the nucleophilic attack feasible.

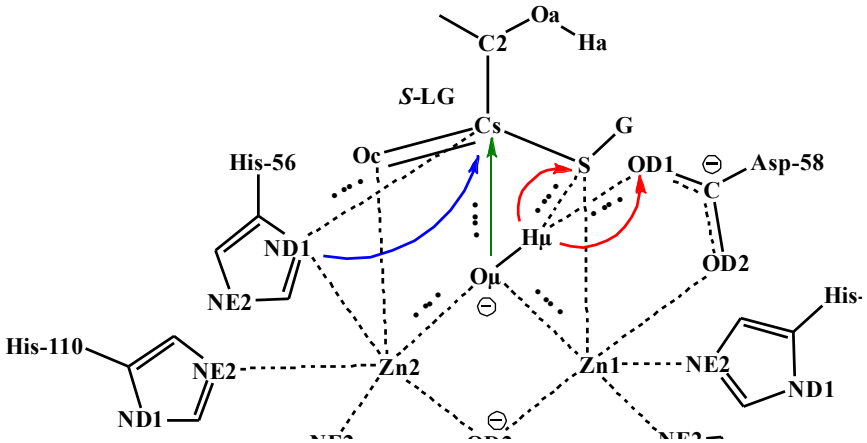

Scheme 5. Schematic view of the **Re** and reasonable reactions from it. Possible and impossible reactions are shown with green and red arrows, respectively, and reactions with high barriers with blue arrows. Selected distances are in Å.

The optimized structure of the product of the Oμ to Cs reaction (**IM1**) is shown in Figure S10 in the Supporting Information and is schematically shown in Scheme 6a. From **IM1**, there are four possible proton transfers, Ha to S, Hw to S, Hμ to S, and Hμ to OD1 of Asp-58 (cf. Scheme 6a). The first three reactions would protonate the S atom, cleave the Cs–S bond and release an H-SG group. The results show that the Hw to S and Ha to S proton transfers have high barriers (19.4 and 18.8 kcal/mol, respectively). On the other hand, the Hμ to OD1 reaction has a very low barrier (0.8 kcal/mol) and reaches an intermediate (**IM2**; its optimized structure is shown in Figure S11 in the Supporting Information and is schematically shown in Scheme 6b). The Hμ to S reaction directly produces the product state (**P**), which is 3.4 kcal/mol higher than **Re**, and the barrier of this reaction is 13.2 kcal/mol. Hence, we can conclude that the Hw to S and Ha to S reactions are unlikely owing to their high barriers (all shown in Figure 2).

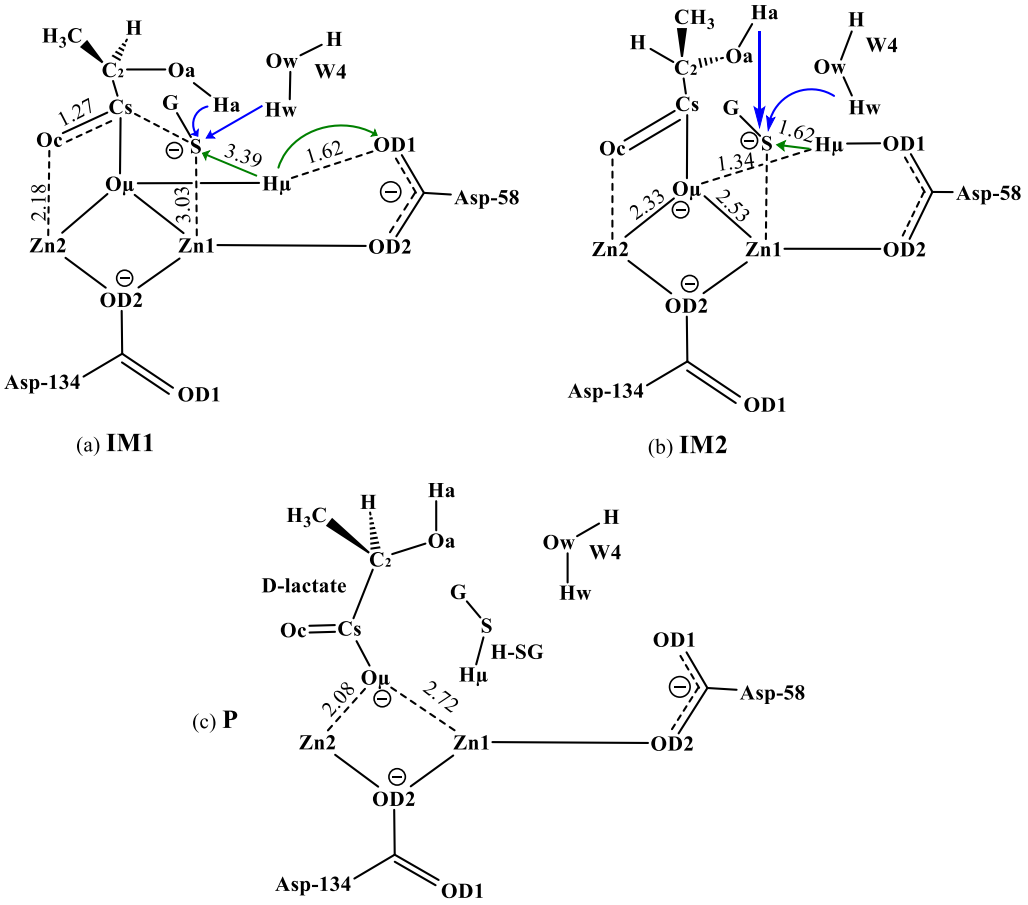

Scheme 6. Schematic view of (a) **IM1**, (b) **IM2**, and (c) **P** and reasonable proton transfers from them. Selected distances are shown in Å. Green arrows indicate likely reactions and blue arrows show reactions with high barriers.

From **IM2**, there are three possible proton transfers, Ha to S, Hw to S, and Hμ to S (cf. Scheme 6b). The results show that the Hw to S and Ha to S proton transfers have high barriers (18.4 and 18.0 kcal/mol, respectively). On the other hand, the Hμ to S reaction has a lower barrier of 12.4 kcal/mol. Hence, we can conclude that in **IM2**, Hμ to S is the most likely reaction (cf. Figure 2). This reaction produces D-lactate and H-SG in the active site, the **P** state (cf. Figure S12 in the Supporting Information and Scheme 6c).

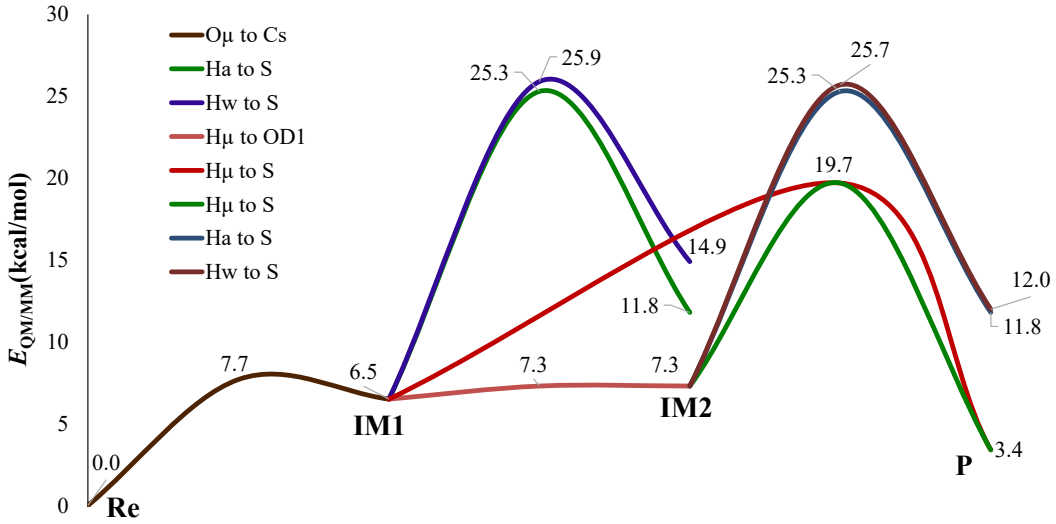

Figure 2. Overall energy profile for all reasonable reactions from **Re** with PS-I.

Our calculations show two alternative paths from **Re** to **P** with the same overall barrier of 19.7 kcal/mol. These paths are Oμ to Cs → Hμ to OD1 → Hμ to S (path1) and Oμ to Cs → Hμ to S (path2). Both paths start with the nucleophilic attack of Oμ on Cs, like Cameron, Makaroff and Himo's mechanisms (cf. Scheme 3 and Scheme 4). The second step of path1 (Hμ to OD1) is also the same as that of Himo's mechanism. However, the last step in Himo's work (breaking the Cs–S bond) is not the same as in our paths. In fact, in our optimized structure of the **Re** state, the S atom is coordinated to Zn1, and the Cs–S bond is cleaved concurrently with transferring Hμ to OD1 in the first path (this also happens concurrently with transferring Hμ to S in the second path). Path2 has only two steps and directly reaches from **IM1** to **P** by the transfer of Hμ to S.

In summary, we propose a reaction mechanism for the GlxII reaction, as shown in Scheme 7. First, Oμ makes a nucleophilic attack on Cs, producing **IM1**. After that, there are two alternative paths to produce the product, one with direct proton transfer of Hμ to S and the other with the consecutive transfers of the Hμ to OD1 and then Hμ to S.

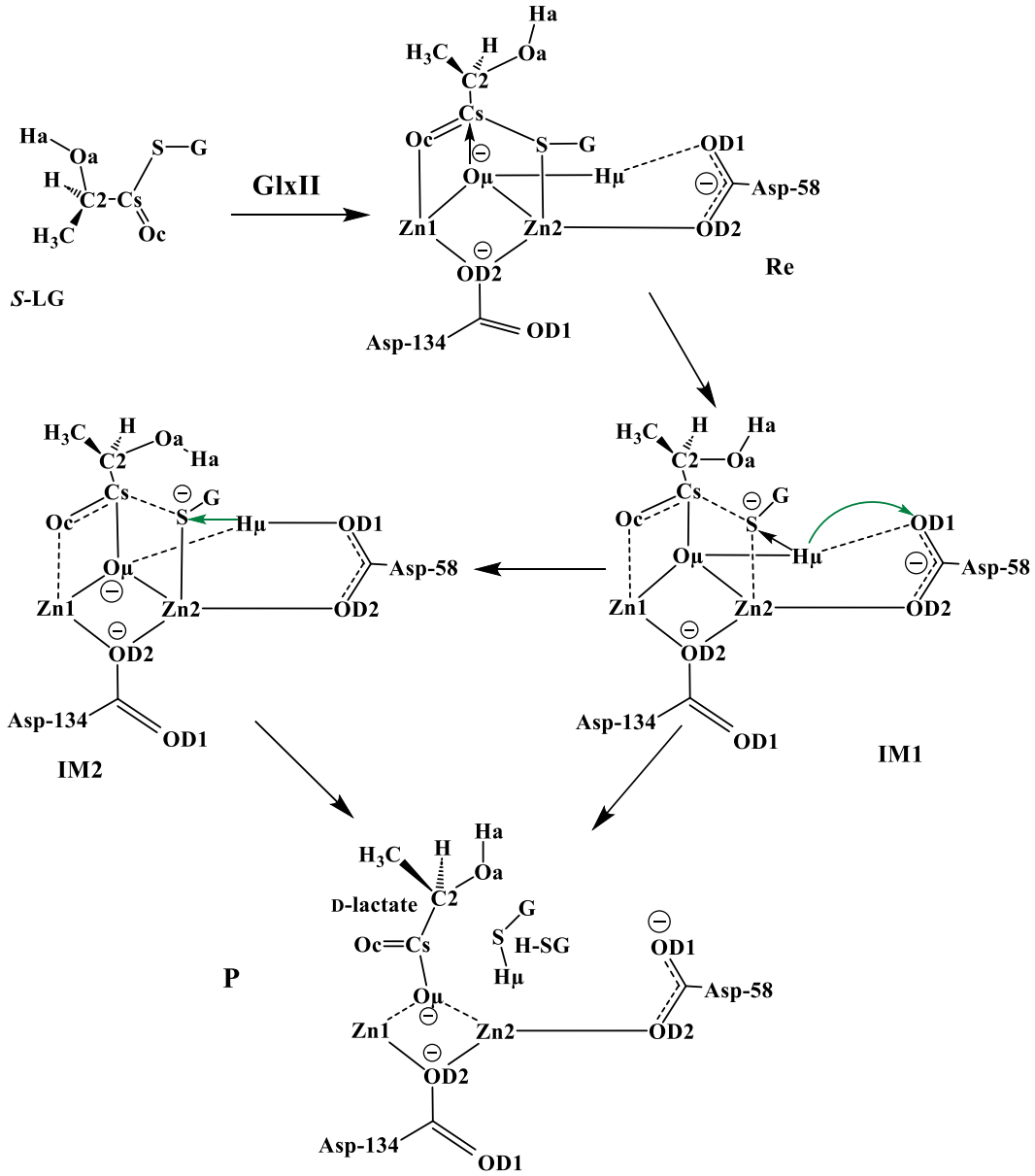

Scheme 7. Our proposed mechanism for the hydrolysis of *S*-D-lactoylglutathione by GlxII.

To improve the quality of the calculated energies for the two alternative paths and to obtain free energy barriers to compare with experimental data, we performed big-QM and QTCP calculations for all stationary points along the two alternative reaction paths and obtained total ΔG_{tot} energies according to Eq. 3.

$$\Delta G_{\mathrm{tot}} = \Delta G_{\mathrm{QTCP}} + E_{\mathrm{big-QM}}^{\mathrm{TZVPD}} - E_{\mathrm{QM/MM}} \qquad (3)$$

The ΔG_{tot} energies of the two alternative paths are plotted in Figure 3. As can be seen, the overall ΔG_{tot} free-energy barriers for path1 and path2 are 13.6 and 13.2 kcal/mol, respectively. GlxII has a catalytic turnover number (k_{cat}) of 2.8 $\times 10^2$ s^{-1} and a k_{cat}/K_m (K_m is the Michaelis constant) value of 8.8 $\times 10^5$ M^{-1} s^{-1} for its substrate *S*-LG.[117] The k_{cat}/K_m is very large and close to the diffusion limit. The k_{cat} value corresponds to a barrier of ~14 kcal/mol according to classical transition-state theory. This shows that our calculated overall barriers are in excellent agreement with the experiments. Furthermore, the GlxII reaction with *S*-LG as the substrate shows only a small solvent-isotope effect, $k_{cat}(H_2O)/k_{cat}(D_2O)$

= 1.24 and $K_m(H_2O)/K_m(D_2O)$ = 1.42. These results suggest that general acid-general base catalysis is not the rate-determining step (RDS). According to Figure 3, the RDS of path1 and path2 are Hμ to S (the green profile in Figure 3) and Oμ to Cs (the blue profile in Figure 3) reactions, respectively. Therefore, we conclude that path2 in our proposed mechanism (which has the lower calculated barrier) agrees with the experimental data since a hydrogen-containing bond is not formed or broken during RDS.

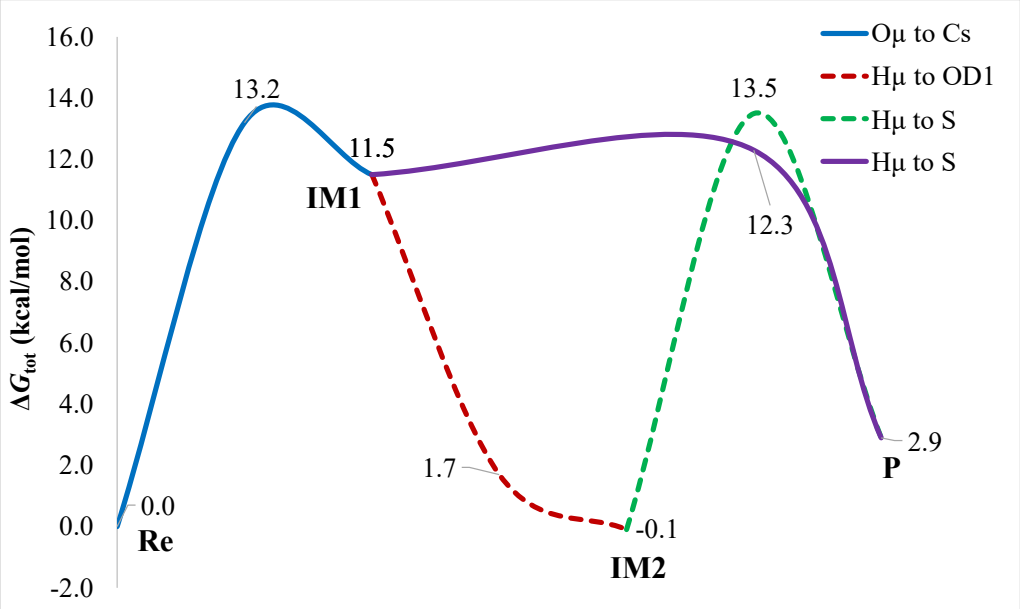

Figure 3. The ΔG_{tot} energy profile of the two alternative reaction paths. The first profile (blue line) is common for the two paths. The preceding steps of path1 and path2 are shown with dashed and solid lines, respectively. The energy components of the profiles are shown in Table S3 in the Supporting Information.

Table 2. Distances between the atoms directly involved in the reaction (Å). The first row shows the protonation state of each structure according to Table 1.

Distance	PS-I **Re**	PS-I **IM1**	PS-I **IM2**	PS-I **P**	PS-II **Re**	PS-III **Re**	PS-IV **Re**	PS-V **Re**	PS-VI **Re**[a]	PS-VII **Re**	PS-VIII **Re**
Cs-S	1.81	2.09	2.84	3.10	1.78	1.82	1.79	3.03	1.78	2.87	1.83
Cs-Oc	1.22	1.27	1.25	1.24	1.23	1.21	1.23	1.24	1.23	1.25	1.21
Cs-Oμ	2.61	1.50	1.33	1.31	2.56	2.90	2.68	1.30	2.67	1.32	2.87
S-Zn1	3.54	3.03	2.53	3.71	3.32	3.80	3.20	2.50	3.45	2.48	3.39
Oc-Zn2	2.84	2.18	2.23	2.65	2.94	2.96	2.95	2.57	3.14	2.53	2.91
Oμ-Zn1	2.03	2.23	2.53	2.71	2.00	2.14	1.97	2.98	2.04	2.24	2.21
Oμ-Zn2	2.01	2.27	2.33	2.08	1.96	2.08	1.95	2.03	1.97	2.03	2.16
Zn1-Zn2	3.17	3.36	3.36	3.40	3.16	3.29	3.48	3.49	3.16	3.54	3.39
Cs-ND1[b]	3.87	3.41	3.07	3.04	4.04	3.82	3.92	3.21	4.13	3.27	3.86
Oμ-Hμ	0.99	1.03	1.34	2.12	0.99	0.96	1.00	-	0.99	-	1.07
Hμ-OD1[c]	1.79	1.62	1.14	3.96	1.78	2.82	1.78	-	1.83	-	1.46

[a] Hμ, in this case, is the proton added to OD1 of Asp-58.
[b] ND1 of His-56.
[c] OD1 of Asp-58.

3.2 Effect of the protonation states of some active site groups

In this section, we study effects of variations in the protonation states of Asp-29 (a buried charged residue with no nearby oppositely charged residue in the enzyme), Asp-58 (a Zn1 ligand), Asp-134 (the ligand bridging the two Zn ions), Oμ (the other ligand bridging the Zn ions). The effect of the protonation state of these groups on the mechanism of the reaction is unknown. Further, assigning

appropriate protonation states to active site residues is key to obtain reliable reaction mehcanisms and accurate reaction energeics, especially when the residues are located at the active site.[118] Though in many cases, protonation states can be predicted by a visual inspection, in some cases, MD simulations and QM/MM calculations are necessary to determine the protonation state.[118–120] In the following, we perform QM/MM calculations to obtain the energetics of the conceivable reactions with alternative protonation states (the results of QM/MM calculations are summarized in Table S4 in the Supporting Information) and study their effect on the local structure of the active site by MD simulations.

3.2.1 Effect of protonation of Asp-29

Asp-29 is a buried residue close to the active site that does not form any ionic pair with any other residue. The distances of the OD2 atom of this residue to the Zn1 and Zn2 ions are 7.15 and 7.99 Å (the position of this residue with respect to the active site is shown in Figure 4). This residue does not participate directly in the reaction but may affect it electrostatically. In the results of the previous section, Asp-29 was deprotonated and, therefore, negatively charged. We neutralized this residue by protonating it on its OD2 atom (PS-II in Table 1) and rerun the reactions starting from the reactant state, shown in Scheme 5 (nucleophilic attack of Oμ on Cs, transfer of Hμ to OD1 of Asp-58, and transfer of Hμ to S). Our calculations showed that the two first reactions are not possible (the atoms return to the starting point after releasing any constraints). In addition, the last reaction (Hμ to S) has a high activation energy (37.8 kcal/mol), making it impossible. These results imply that a charged Asp-29 is necessary for making the GlxII reaction possible.

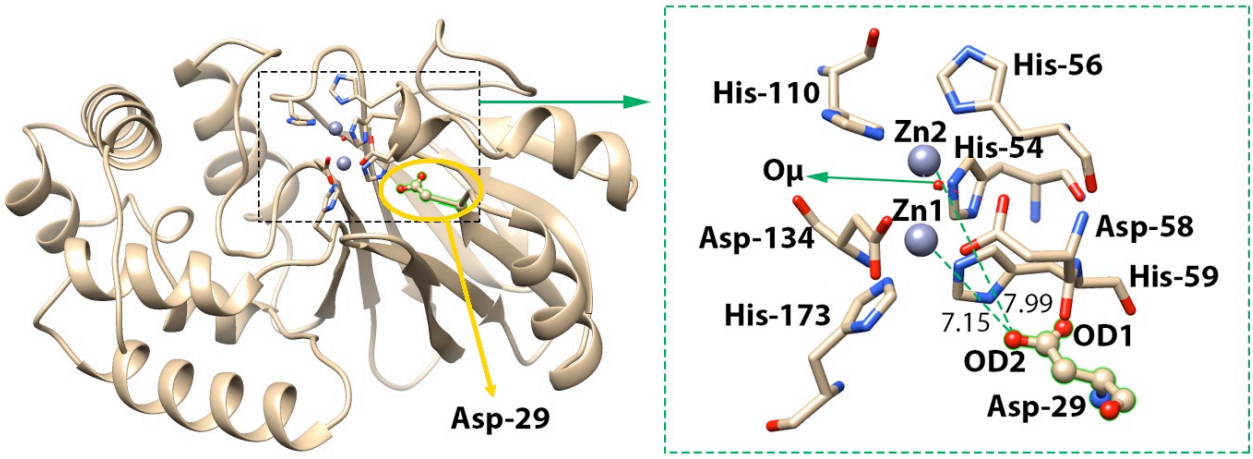

Figure 4. The position of Asp-29 in the active site of the enzyme. Selected distances are in Å. The figure was constructed with UCSF Chimera, developed by the Resource for Biocomputing, Visualization, and Informatics at the University of California, San Francisco, with support from NIH P41-GM103311.[121]

A buried charge not forming an ionic pair (Asp-29) is unusual inside proteins. To check if this is reasonable, we conducted MD simulations to investigate whether it disturbs the surrounding structure or not. MD simulations are an effective tool for assigning the correct protonation states to protein residues.[118–120] We performed three sets of MD simulations, in which Asp-29 was charged, protonated on OD1, or protonated on OD2 (called simulations I, II-1, and II-2, respectively). In each

simulation, we analyzed the mass-weighted RMSDs of heavy atoms of active site residues in chain A from the positions observed in the crystal structure and summarized them in Table 3. If an incorrect protonation state is used, atoms in that residue or in nearby residues may move to release steric or electrostatic clashes or to form new favorable interactions. As a result, the RMSD will be higher for incorrect protonation states. According to Table 3, the RMSD of Asp-29 is lower if it is deprotonated than if it is protonated (0.13 vs. 0.18–0.35 Å; compare the values in the second row of Table 3 with those in rows 3 and 4). On the other hand, neutralizing Asp-29 does not significantly affect the RMSDs of His-54 and His-56 (7th and 8th columns of Table 3). This is not surprising since these histidine residues coordinate to Zn2, which is located far from Asp-29 (cf. Figure 4). Similarly, the RMSD values of His-110, Asp-134, and His-173 are not affected by the protonation state of Asp-29 (0.18, 0.13, and 0.17 Å, respectively). The RMSDs of Asp-58 and His-59 are slightly lower when Asp-29 is charged (0.18–0.23 vs. 0.14 Å for Asp-58 and 0.30–0.32 vs. 0.12 Å for His59). This is also natural because these two residues are the closest ones to Asp-29 in the active site (cf. Figure 4).

Based on these results, we conclude that Asp-29 is charged in the crystal structure of GlxII and that a charged Asp-29 is necessary for the catalytic reaction. Additionally, the results demonstrate the capability of MD simulation in assigning the correct protonation states to the active site residues. In a similar way, we have shown in a recent study that the protonation state of Glu-464 plays a crucial role in the catalytic process of myrosinase.[118] Another result of the present analysis is that when there is a buried charge that does not form any ion pair near the active site, it has to be considered thoroughly by MD simulations or QM/MM calculations to identify its correct protonation state.

Table 3. Mass-weighted RMSD values in Å in the nine MD simulations with different protonation states of Asp-29, Asp-58, Asp-134, and Oμ (PS-I to PS-VIII). The protonated atoms of these residues during the simulations are shown in columns 2–5. RMSDs were calculated for the heavy atoms of the active site residues in chain A. The data in the last column are the average difference (Av diff) of the results from that of PS-I. Entries in bold face are at least 0.04 Å larger than those of PS-I.

PS	Asp-29	Asp-58	Asp-134	Oμ	Asp-29	His-54	His-56	Asp-58	His-59	His-110	Asp-134	His-173	Av diff
I	None	None	None	OH^-	0.13	0.15	0.15	0.14	0.12	0.18	0.13	0.17	
II-1	OD1	None	None	OH^-	**0.35**	0.15	0.15	**0.23**	**0.30**	0.18	0.13	0.17	**0.06**
II-2	OD2	None	None	OH^-	**0.18**	0.16	0.15	**0.18**	**0.32**	0.18	0.13	0.17	**0.04**
III	None	OD1	None	OH^-	0.13	0.16	0.14	**0.24**	0.12	0.17	0.12	0.16	0.01
IV	None	None	OD1	OH^-	0.12	0.15	0.14	0.15	0.14	0.20	**0.86**	0.14	**0.09**
V	None	None	None	O^{2-}	0.12	0.17	0.14	0.17	0.12	0.21	0.15	0.18	0.01
VI	None	OD1	None	O^{2-}	0.13	0.17	0.14	0.16	0.14	0.18	0.16	0.16	0.01
VII	None	None	OD1	O^{2-}	0.12	0.18	0.15	**0.72**	0.15	0.20	**0.31**	0.18	**0.11**
VIII	None	None	None	OH_2	0.12	0.15	0.14	0.16	0.14	0.19	0.12	0.16	0.00

3.2.2 Effect of protonation of Asp-58

Asp-58 is an important active site residue that directly participates in the catalytic reaction as a general base, abstracting Hμ from Oμ in **IM1** (cf. Scheme 7). Moreover, it makes a hydrogen-bond bridge via Hμ to Oμ in **Re** (cf. Figure 1) and affects the first reaction step (nucleophilic attack of Oμ

on Cs), stabilizing **IM1** by making this strong hydrogen bond (the OD1–Hμ distance in **Re** and **IM1** are 1.79 and 1.62 Å, respectively; cf. Table 2). To study the effects of this residue further, we protonated it on the OD1 atom (the OD2 atom coordinates to Zn1) and rerun the reaction from the **Re** state. The optimized structure of the **Re** state with protonated Asp-58 (PS-III) is shown in Figure S2 in the Supporting Information and is schematically represented in Scheme 8. There are three possible reactions as the first step of the reaction, viz., transfer of Hμ to S, nucleophilic attack of Oμ on Cs, and transfer of Hd of Asp-58 to S (cf. Scheme 8). Our calculations showed that the first reaction (Hμ to S) is impossible (the atoms return to the starting point after releasing any constraints). In addition, the two latter reactions (Hd to S and Oμ to Cs) have high activation energies of 44.5 and 24.4 kcal/mol, respectively, making them prohibitive. Thus, neutralizing Asp-58 deactivates the enzyme.

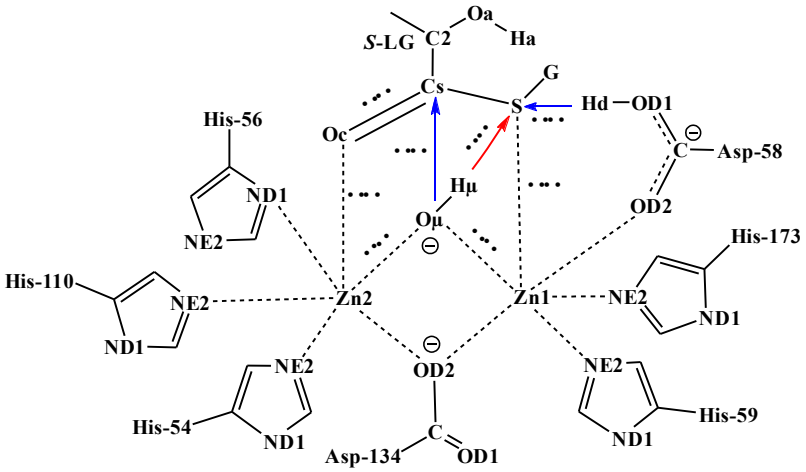

Scheme 8. Schematic view of the **Re** state with PS-III (when Asp-58 is protonated). The impossible reaction is shown with red arrows and reactions with high barriers with blue arrows.

To further investigate the effects of protonation of Asp-58, we conducted an MD simulation and summarized the RMSD values in Table 3 (simulation III). The results indicate that protonating Asp-58 does not affect the RMSD values of the active site residues (the differences in the RMSDs are below 0.01 Å; compare the values in the 2nd and 5th rows in Table 3). The only exception is that of Asp-58 itself, the RMSD of which increases from 0.14 to 0.24 Å. Thus, Asp-58 is most likely charged in the crystal structure.

3.2.3 Effect of protonation of Asp-134

Asp-134 is another important residue in the active site of GlxII. In contrast to Asp-58, it does not participate directly in the catalytic reaction. However, it is a bridging ligand between the two Zn ions. To study its effects on the catalytic reaction, we protonated it on the OD1 atom (OD2 coordinates to the two Zn ions) and redid the QM/MM calculations. The optimized structure of the **Re** state with protonated Asp-134 (PS-IV) is shown in Figure S3 in the Supporting Information and schematically represented in Scheme 9. There are four possible reactions as the first step of the reaction, viz., transfer of Hc (the added proton on Asp-134) from OD1 of Asp-134 to S, nucleophilic attack of Oμ on Cs,

transfer of Hμ to S, and transfer of Hμ to OD1 of Asp-58. Our calculations showed that the first reaction (Hc to S) has a high activation energy of 32.4 kcal/mol, making it impossible. In addition, the three last reactions (Oμ to Cs, Hμ to S, and Hμ to OD1) are not possible because the atoms return to the starting point after releasing any bond constraints.

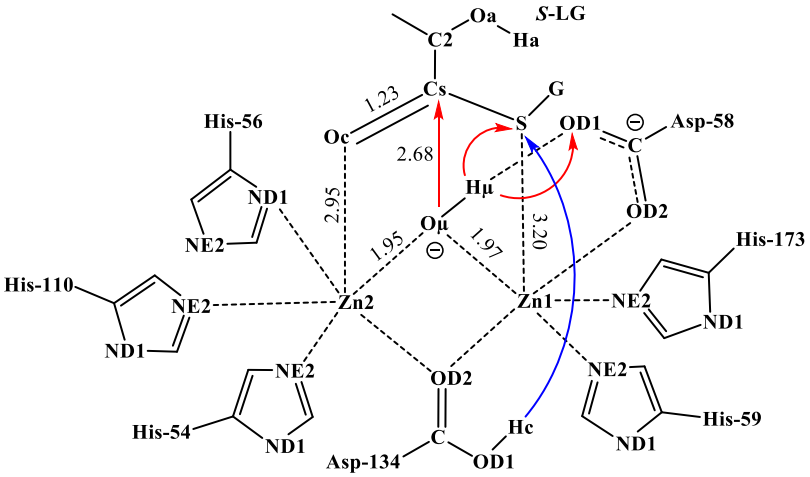

Scheme 9. Schematic view of the **Re** state with PS-IV (when Asp-134 is protonated). The impossible reactions are shown with red arrows and the reaction with a high barrier with the blue arrow.

We performed an MD simulation to examine further the effects of the protonation of Asp-134 on the local structure of the protein in the active site. According to the results in Table 3 (simulation IV), protonating Asp-134 does not significantly affect the RMSDs of active site residues, except that of Asp-134 itself, which increases significantly from 0.13 to 0.86 Å.-In conclusion, the MD simulations indicate that Asp-134 is protonated in the crystal structure of GlxII.

3.2.4 Changing the bridging hydroxide to an oxide ion

The bridging hydroxide ion is an important ligand that plays a key role in the reaction (cf. Scheme 7). This group is present in the crystal structure as HOH-466 crystal water in chain B. So far, we modeled this group as a hydroxide ion. It is possible that this group instead is an oxide ion or a water molecule since the crystal structure does not show any hydrogen atoms. In this section, we modeled this group as an oxide ion and examined possible reactions from the **Re** state. As shown in the optimized structure of the **Re** state, when the bridging hydroxide is changed to an oxide ion (Scheme 10 and Figure S4 in the Supporting Information), the *S*-LG's Cs–S bond is cleave, and a Cs–Oμ bond is formed, indicating that the first step of the catalytic reaction takes place as soon as the substrate enters the active site of the enzyme, producing a D-lactate ion. For H-SG to be generated, there are six possible reactions from this stationary point, viz., coordination of Ow1 of W1 to Zn1, coordination of Ow2 of W2 to Zn2, transfer of Hw1 from W1 to S, transfer of Hw2 from W1 to S, transfer of Ha from Oa to S, and transfer of Hw1 from W1 to Oμ. Our calculations showed that the five first reactions (Ow1 to Zn1, Ow2 to Zn2, Hw1 to S, Hw2 to S, and Ha to S) are impossible because the atoms return to the starting point after releasing any bond constraints. Transferring Hw1 from W1 to Oμ is impossible because of its high activation energy (39.8 kcal/mol). In summary, if the bridging oxygen

is an oxide ion, it will produce lactate and deprotonated H-SG immediately after entering the substrate into the active site. However, the reaction cannot proceed further.

Moreover, we are not sure if the oxide ion is the stable form of the bridging oxygen or not. Therefore, we run an MD simulation with this protonation state. The results in Table 3 (simulation V) show that the change of the bridging hydroxide ion to the oxide ion affects the RMSDs of the active site residues only slightly (it increases for four of them by 0.01–0.03 Å, whereas it decreases for two by 0.01 Å; average change 0.01 Å). Thus, there is only a slight preference for a bridging OH^- group.

On the other hand, the QM/MM optimized structure of the **Re** state is much closer to the crystal structure when the bridging oxygen is an OH^- group. In particular, the Zn1–Oμ and Zn2–Oμ distances in the crystal structure are 2.09 and 2.01 Å (averaged over the two subunits), which are much closer to the distances in the QM/MM optimized **Re** structure with an OH^- group (2.03 and 2.01 Å) than with an O^{2-} group (2.98 and 2.03 Å). These results confirm that Oμ is OH^- in the crystal structure. The QM/MM results also show that the reaction only proceeds when the active site residues are in the correct protonation state.

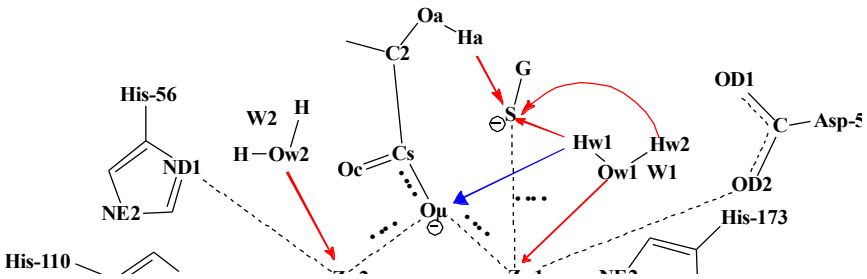

Scheme 10. Schematic view of the **Re** state with PS-V (when the bridging hydroxide is changed to an oxide ion). Impossible reactions are shown with red arrows and reaction with a high barrier with a blue arrow.

3.2.5 Changing the bridging hydroxide to an oxide ion and protonating Asp-58

Next, we tried to protonate Asp-58 while keeping the bridging oxygen as an oxide ion (PS-VI). This means transferring Hμ from Oμ in PS-I to Asp-58. As shown in the optimized structure of the **Re** state with this protonation state (Figure S5 in the Supporting Information), the added proton from OD1 is automatically transferred to the oxide ion regenerating the original PS-I **Re** state (Scheme 5). This also shows that the hydroxide ion is the more stable state of the bridging ligand.

QM/MM calculations indicate that the **Re** state with an O_2^- bridging group and a protonated Asp-58 is 10.6 kcal/mol less stable when the bridging oxygen is an OH^- (this energy was obtained by constraining the H–OD1 distance to 1.0 Å). This protonation state only slightly affects the RMSDs of active site residues (average change 0.01 Å; simulation VI in Table 3).

3.2.6 Changing the bridging hydroxide to an oxide ion and protonating Asp-134

We also tested modeling the bridging oxygen as an oxide ion and protonating Asp-134 (PS-VII). Both of these groups are bridging Zn ligands. In the optimized structure of this QM system (Scheme 11 and Figure S6 in the Supporting Information), the Cs–S bond of *S*-LG is cleaved, producing a lactate ion and an –SG group coordinating to the Zn1 ion. Furthermore, the Cs–Oμ bond is formed, indicating that the reaction is carried out as soon as the substrate enters the active site. To produce H-SG and dissociate the –SG group from the Zn1 ion, there are six possible reactions as the first step of the reaction, viz., coordination of Ow1 of W1 to Zn1, transfer of Hw1 from the W1 to S, transfer of Hw2 from the W1 to S, transfer of Hw1 from the W1 to Oμ, transfer of Hc from OD1 of the Asp-134 to Oμ, and transfer of Hc from OD1 of the Asp-134 to S. These are shown in Scheme 11.

Our calculations showed that the four first reactions (Ow1 to Zn1, Hw1 to S, Hw2 to S, and Hw1 to Oμ) are impossible, because the atoms return to the starting point after releasing any bond constraints. The transfer of Hc from OD1 of the Asp-134 to Oμ has a high energy barrier (33.7 kcal/mol), which makes it unlikely. However, the last reaction (Hc to S) can take place with a barrier and a reaction energy of 10.0 and –18.1 kcal/mol, respectively. This results in the formation of H-SG and lactate. The optimized structure of the product of this reaction is shown in Figure S13 in the Supporting Information. Thus, the reaction from the **Re** state with PS-VII has a lower barrier than the reaction from the original **Re** with PS-I (barriers of 10.0 vs. 19.7 kcal/mol in QM/MM energy term). On the other hand, the **Re** state with PS-VII (Hμ on Asp-134) is 16.5 kcal/mol less stable than the **Re** state with PS-I (Hμ on Oμ). By adding this value to the barrier from the **Re** state with PS-VII, the overall barrier becomes 26.5 kcal/mol, making this reaction unlikely. MD simulations with this protonation state (simulation VII) do not affect the RMSDs for Asp-29, His-59, and His-110. However, those of Asp-58 and Asp-134 are strongly increased (to 0.72 and 0.31 Å), showing that this is an unlikely protonation state.

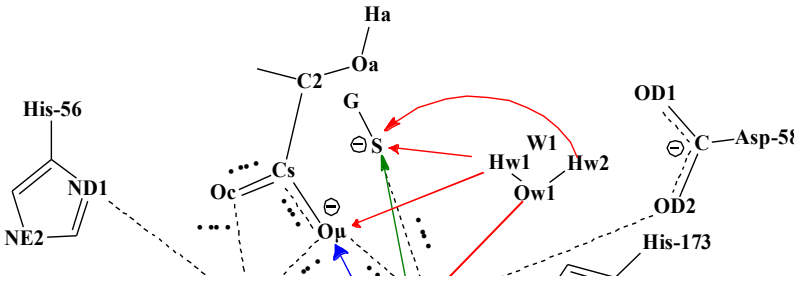

Scheme 11. Schematic view of the **Re** with PS-VII (when the bridging oxygen as O^{2-} and Asp-134 protonated). Possible and impossible reactions are shown with green and red arrows, respectively, and reactions with high barriers with blue arrows.

3.2.7 Changing the bridging hydroxide to water

Finally, we tested the effect of changing the bridging oxygen to a water molecule. The optimized structure of the **Re** state with a bridging H_2O group (PS-VIII) is shown in Figure S7 in the Supporting Information and is schematically represented in Scheme 12. There are six possible reactions from it, viz., transfer of Hμ1 to S, transfer of Hμ1 to OD1 of Asp-134, nucleophilic attack of Oμ on Cs, transfer of Hμ2 to OD1 of Asp-58, transfer of Ha from Oa to S, and transfer of Hμ1 to Oc (Hμ1 and Hμ2 are the hydrogen atoms of the bridging H_2O). These are shown in Scheme 12. Our calculations showed that the first two reactions (Hμ1 to S and Hμ1 to OD1 of Asp-134) have high activation energies (23.1 and 29.7 kcal/mol, respectively), making them prohibitive. In addition, the four latter reactions (Oμ to Cs, Hμ2 to OD1 of Asp-58, Ha to S, and Hμ1 to Oc) are not possible because the atoms return to the starting point after releasing any bond constraints. Thus, none of the reactions are possible, and there is no reaction path from the **Re** state with a bridging H_2O group.

In addition, changing the protonation state of Oμ from OH^- to H_2O leads to poorer Zn–Oμ distances: The Zn1–Oμ and Zn2–Oμ distances in the **Re** state with H_2O are 2.21 and 2.16 Å, which are quite far from those in the crystal structure, 2.09 and 2.01 Å, compared to the QM/MM structure with OH^-, 2.03 and 2.01 Å). The RMSDs of the active site residues are not significantly affected if the MD simulations are run with a bridging H_2O group (simulation VIII in Table 3).

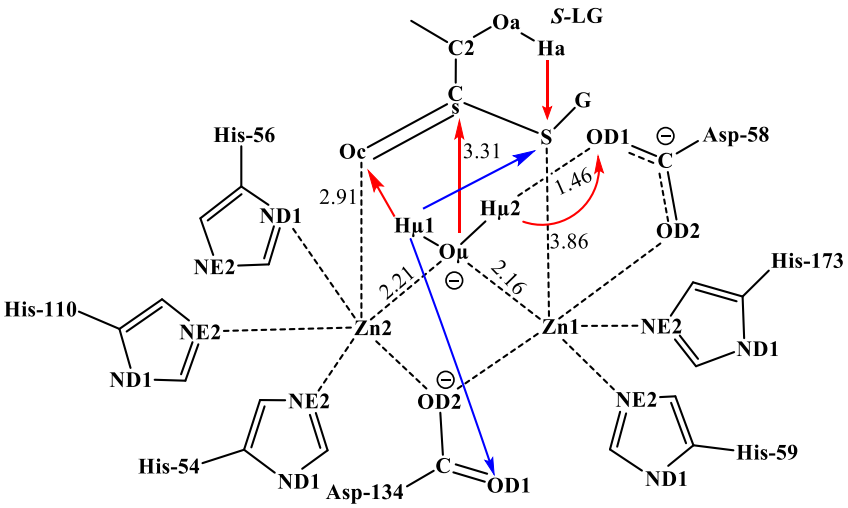

Scheme 12. Schematic view of the **Re** with PS-VIII (with a bridging H_2O group). Impossible reactions are shown with red arrows and reactions with high barriers with blue arrows.

4. Conclusions

We have studied the catalytic reaction mechanism of human GlxII, a binuclear metalloenzyme with two Zn ions in its active site. We have examined previously proposed reaction mechanisms and all reasonable reactions from stationary structures along the reaction path. We used the QM/MM method, which involves modeling the entire enzyme to provide accurate geometries and energies. Moreover, we performed big-QM and QTCP calculations further to improve the quality of the calculated energy profile. We reject the previously proposed VJ mechanism and propose somewhat different reaction steps compared to Himo's mechanism. Our mechanism is shown in Scheme 7 and the calculated reaction energies agree with the experimental data, thus demonstrating the reliability of the reported energies and the proposed reaction mechanism.

Moreover, we examined the effects of the protonation states of Asp-29, Asp-58, Asp-134, and Oμ on the catalytic reaction. As was observed with myrosinase,[118] protonation states of active site residues can significantly affect energetics and even the possibility of the reaction. On the other hand, changing a protonation state may also accelerate the reaction. Therefore, it is crucial to correctly assign the protonation state of active site residues using sophisticated tools, such as MD simulations and comparing the obtained QM/MM geometries with available crystal structures.

We first examined the effect of different protonation states on Asp-29, a residue that is buried close to the active site (cf. Figure 4). From the **Re** state in which Asp-29 is protonated, no intermediate or product could be identified through QM/MM calculations. Additionally, MD simulations using protonated Asp-29 show higher RMSDs for this residue and some active site residues, suggesting that it is charged in the crystal structure. This illustrates the ability of MD simulations to determine the protonation state of protein residues accurately. It also shows that a buried charge that does not form an ionic pair near the active site may significantly affect the catalytic reaction.

QM/MM calculations also indicate that protonated Asp-58 or Asp-134 prevent GlxII from

catalyzing the reaction. MD simulations show higher RMSDs for these aspartic residues when they are protonated. However, protonating these residues does not increase the RMSDs of other active site residues.

In addition, we tried to replace the bridging hydroxide ion with an oxide ion. This led to a barrierless reaction, producing D-lactate and SG^- as soon as the substrate was introduced into the active site. However, the enzyme cannot pass a proton to SG^-. When comparing Zn–ligand distances in the optimized QM/MM **Re** structure with those in the crystal structure, it is evident that the optimized structure with the OH^- group is much closer to the crystal structure than that with O^{2-}. This strongly suggests that the bridging group is OH^- in the crystal structure. QM/MM **Re** structures with O^{2-} as the bridging group and Asp-58 or Asp-134 protonated, were found to be 10.6 and 16.5 kcal/mol less stable than structures with OH^-, respectively. Likewise, calculations with a bridging H_2O group showed that no reaction was possible and that the QM/MM **Re** structure reproduces the crystal structure worse than if the bridging group is OH^-.

In summary, we propose a novel mechanism for the GlxII catalytic reaction. We also demonstrate that assigning correct protonation states of active site residues of GlxII is a determining factor for investigating its enzymatic reaction mechanism, and that QM/MM optimized structures and MD simulations can serve this purpose effectively. Similar conclusions has been reached also for other enzymes. For example, Merz et al. showed that correctly assigning the protonation state of an active site residue (Asp-86) of dizinc-β-lactamase is critical both kinetically and thermodynamically for its reaction.[53] In addition, it was indicated that the correct protonation state of Asp-120 in the active site of metallo-β-lactamase from *Bacteroides fragilis* is crucial for its mechanism of action.[122]

Supporting Information Available

A brief overview of the reaction mechanism of several binuclear zinc enzymes, optimized structures of **Re** states with different protonation states of some active site residues; the big-QM system and structures of **IM1**, **IM2,** and **P**; further details of the QTCP calculations; the optimized model used to calculate charges for the MM force field; MM charges, force constants and restraints used for the Zn clusters; optimized structure of the product of the Hc to S reaction with an O^{2-} bridging group and a protonated Asp-134, energy components of ΔG_{tot}, the plot of the kinetic, potential, and total energy of PS-I versus time in the MD simulations, the plot of the time dependence of the RMSD for the protein, the scan profiles for the Oμ to Cs, Hμ to OD1, and Hμ to S distances, QM/MM, Big-QM energy profiles of the two alternative reaction paths, the results summary of QM/MM calculations of the protonation states of some active site groups, force field parameters for H-SG and GBP and PDB structures showing their atom names,

Acknowledgments

This investigation has been supported by grants from the Swedish research council (project 2018-05003) and the Vice President for Research and Technology, University of Kurdistan (project 01/9/3778). The computations were performed on computer resources provided by the Swedish National Infrastructure for Computing (SNIC) at Lunarc at Lund University and HPC2N at Umeå University, partially funded by the Swedish Research Council (grant 2018-05973).

5. References

(1) Thornalley, P. J. The Glyoxalase System in Health and Disease. *Mol. Aspects Med.* **1993**, *14* (4), 287–371.
(2) Shibamoto, T. Analytical Methods for Trace Levels of Reactive Carbonyl Compounds Formed in Lipid Peroxidation Systems. *J. Pharm. Biomed. Anal.* **2006**, *41* (1), 12–25.
(3) Kalapos, M. P. The Tandem of Free Radicals and Methylglyoxal. *Chem. Biol. Interact.* **2008**, *171* (3), 251–271.
(4) Ohmori, S.; Mori, M.; Shiraha, K.; Kawase, M. Biosynthesis and Degradation of Methylglyoxal in Animals. *Prog. Clin. Biol. Res.* **1989**, *290*, 397–412.
(5) Hiraku, Y.; Sugimoto, J.; Yamaguchi, T.; Kawanishi, S. Oxidative DNA Damage Induced by Aminoacetone, an Amino Acid Metabolite. *Arch. Biochem. Biophys.* **1999**, *365* (1), 62–70.
(6) Dutra, F.; Knudsen, F. S.; Curi, D.; Bechara, E. J. H. Aerobic Oxidation of Aminoacetone, a Threonine Catabolite: Iron Catalysis and Coupled Iron Release from Ferritin. *Chem. Res. Toxicol.* **2001**, *14* (9), 1323–1329.
(7) Hopkins, F. G.; Morgan, E. J. On the Distribution of Glyoxalase and Glutathione. *Biochem. J.* **1945**, *39* (4), 320.
(8) Kalapos, M. P. Where Does Plasma Methylglyoxal Originate From? *Diabetes Res. Clin. Pract.* **2013**, *99* (3), 260–271.
(9) Vander Jagt, D. L.; Hassebrook, R. K.; Hunsaker, L. A.; Brown, W. M.; Royer, R. E. Metabolism of the 2-Oxoaldehyde Methylglyoxal by Aldose Reductase and by Glyoxalase-I: Roles for Glutathione in Both Enzymes and Implications for Diabetic Complications. *Chem. Biol. Interact.* **2001**, *130*, 549–562.
(10) Neuberg, C. The Destruction of Lactic Aldehyde and Methylglyoxal by Animal Organs. *Biochem Z* **1913**, *49*, 502–506.
(11) Dakin, H. D. Dudley, HW. *J. Biol. Chem.* **1913**, *1913*, 15–263.
(12) Barata, L.; Sousa Silva, M.; Schuldt, L.; Da Costa, G.; Tomás, A. M.; Ferreira, A. E. N.; Weiss, M. S.; Ponces Freire, A.; Cordeiro, C. Cloning, Expression, Purification, Crystallization and Preliminary X-Ray Diffraction Analysis of Glyoxalase I from Leishmania Infantum. *Acta Crystallogr. Sect. F Struct. Biol. Cryst. Commun.* **2010**, *66* (5), 571–574.
(13) Sousa Silva, M.; Barata, L.; Ferreira, A. E. N.; Romão, S.; Tomás, A. M.; Ponces Freire, A.; Cordeiro, C. Catalysis and Structural Properties of Leishmania Infantum Glyoxalase II: Trypanothione Specificity and Phylogeny. *Biochemistry* **2008**, *47* (1), 195–204.
(14) de Arriba, S. G.; Stuchbury, G.; Yarin, J.; Burnell, J.; Loske, C.; Münch, G. Methylglyoxal Impairs Glucose Metabolism and Leads to Energy Depletion in Neuronal Cells—Protection by Carbonyl Scavengers. *Neurobiol. Aging* **2007**, *28* (7), 1044–1050.
(15) Vander Jagt, D. L. Glyoxalase II: Molecular Characteristics, Kinetics and Mechanism. *Biochem. Soc. Trans.* **1993**, *21* (2), 522–527.
(16) Iyengar, R.; Rose, I. A. Concentration of Activated Intermediates of the Fructose-1, 6-Bisphosphate Aldolase and Triosephosphate Isomerase Reactions. *Biochemistry* **1981**, *20* (5), 1223–1229.
(17) Richard, J. P. Kinetic Parameters for the Elimination Reaction Catalyzed by Triosephosphate Isomerase and an Estimation of the Reaction's Physiological Significance. *Biochemistry* **1991**,

30 (18), 4581–4585. https://doi.org/10.1021/bi00232a031.
(18) Lorenzi, M.; Cagliero, E.; Toledo, S. Glucose Toxicity for Human Endothelial Cells in Culture: Delayed Replication, Disturbed Cell Cycle, and Accelerated Death. *Diabetes* **1985**, *34* (7), 621–627.
(19) Lorenzi, M.; Cagliero, E. Pathobiology of Endothelial and Other Vascular Cells in Diabetes Mellitus: Call for Data. *Diabetes* **1991**, *40* (6), 653–659.
(20) Thornalley, P. J.; Strath, M.; Wilson, R. J. M. Antimalarial Activity in Vitro of the Glyoxalase I Inhibitor Diester, Sp-Bromobenzylglutathione Diethyl Ester. *Biochem. Pharmacol.* **1994**, *47* (2), 418–420.
(21) Ridderström, M.; Saccucci, F.; Hellman, U.; Bergman, T.; Principato, G.; Mannervik, B. Molecular Cloning, Heterologous Expression, and Characterization of Human Glyoxalase II. *J. Biol. Chem.* **1996**, *271* (1), 319–323.
(22) Cameron, A. D.; Ridderström, M.; Olin, B.; Mannervik, B. Crystal Structure of Human Glyoxalase II and Its Complex with a Glutathione Thiolester Substrate Analogue. *Structure* **1999**, *7* (9), 1067–1078.
(23) Limphong, P.; Adams, N. E.; Rouhier, M. F.; McKinney, R. M.; Naylor, M.; Bennett, B.; Makaroff, C. A.; Crowder, M. W. Converting GLX2-1 into an Active Glyoxalase II. *Biochemistry* **2010**, *49* (37), 8228–8236.
(24) Inoue, Y.; Maeta, K.; Nomura, W. Glyoxalase System in Yeasts: Structure, Function, and Physiology. In *Seminars in cell & developmental biology*; Elsevier, 2011; Vol. 22, pp 278–284.
(25) Gomes, R. A.; Sousa Silva, M.; Vicente Miranda, H.; Ferreira, A. E. N.; Cordeiro, C. A. A.; Freire, A. P. Protein Glycation in Saccharomyces Cerevisiae: Argpyrimidine Formation and Methylglyoxal Catabolism. *FEBS J.* **2005**, *272* (17), 4521–4531.
(26) Urscher, M.; Deponte, M. Plasmodium Falciparum Glyoxalase II: Theorell-Chance Product Inhibition Patterns, Rate-Limiting Substrate Binding via Arg257/Lys260, and Unmasking of Acid-Base Catalysis. **2009**.
(27) Irsch, T.; Krauth-Siegel, R. L. Glyoxalase II of African Trypanosomes Is Trypanothione-Dependent. *J. Biol. Chem.* **2004**, *279* (21), 22209–22217.
(28) Marasinghe, G. P. K.; Sander, I. M.; Bennett, B.; Periyannan, G.; Yang, K.-W.; Makaroff, C. A.; Crowder, M. W. Structural Studies on a Mitochondrial Glyoxalase II. *J. Biol. Chem.* **2005**, *280* (49), 40668–40675.
(29) Uotila, L. Purification and Characterization of S-2-Hydroxyacylglutathione Hydrolase (Glyoxalase II) from Human Liver. *Biochemistry* **1973**, *12* (20), 3944–3951.
(30) Norton, S. J.; Principato, G. B.; Talesa, V.; Lupattelli, M.; Rosi, G. Glyoxalase II from Zea Mays: Properties and Inhibition Study of the Enzyme Purified Hy Use of a New Affinity Ligand. *Enzyme* **1989**, *42*, 189–196.
(31) Murata, K.; Inoue, Y.; Watanabe, K.; Fukuda, Y.; SADCUSA, T.; Shimosaka, M.; Kimura, A. Metabolism of A-Ketoaldehydes in Yeasts: Purification and Characterization of Glyoxalase II from Saccharomyces Cerevisiae. *Agric. Biol. Chem.* **1986**, *50* (1), 135–142.
(32) Bush, P. E.; Norton, S. J. S-(Nitrocarbobenzoxy) Glutathiones: Potent Competitive Inhibitors of Mammalian Glyoxalase II. *J. Med. Chem.* **1985**, *28* (6), 828–830.
(33) Ball, J. C.; Vander Jagt, D. L. S-2-Hydroxyacylglutathione Hydrolase (Glyoxalase II: Active-Site Mapping of a Nonserine Thiolesterase. *Biochemistry* **1981**, *20* (4), 899–905.
(34) Deswal, R.; Chakaravarty, T. N.; Sopory, S. K. The Glyoxalase System in Higher Plants: Regulation in Growth and Differentiation. *Biochem. Soc. Trans.* **1993**, *21* (2), 527–530.
(35) Ji, X.; Moore, H. D. M.; Russell, R. G. G.; Watts, D. J. CDNA Cloning and Characterization of a Rat Spermatogenesis-Associated Protein Rsp29. *Biochem. Biophys. Res. Commun.* **1997**, *241* (3), 714–719.
(36) Antognelli, C.; Frosini, R.; Santolla, M. F.; Peirce, M. J.; Talesa, V. N. Oleuropein-Induced Apoptosis Is Mediated by Mitochondrial Glyoxalase 2 in NSCLC A549 Cells: A Mechanistic inside and a Possible Novel Nonenzymatic Role for an Ancient Enzyme. *Oxid. Med. Cell. Longev.* **2019**, *2019*.
(37) Maiti, M. K.; Krishnasamy, S.; Owen, H. A. Molecular Characterization of Glyoxalase II from

Arabidopsis Thaliana. *Plant Mol. Biol.* **1997**, *35* (4), 471–481.
(38) Bito, A.; Haider, M.; Briza, P.; Strasser, P.; Breitenbach, M. Heterologous Expression, Purification, and Kinetic Comparison of the Cytoplasmic and Mitochondrial Glyoxalase II Enzymes, Glo2p and Glo4p, from Saccharomyces Cerevisiae. *Protein Expr. Purif.* **1999**, *17* (3), 456–464.
(39) Saxena, M.; Bisht, R.; Roy, S. D.; Sopory, S. K.; Bhalla-Sarin, N. Cloning and Characterization of a Mitochondrial Glyoxalase II from Brassica Juncea That Is Upregulated by NaCl, Zn, and ABA. *Biochem. Biophys. Res. Commun.* **2005**, *336* (3), 813–819.
(40) Xue, M.; Rabbani, N.; Momiji, H.; Imbasi, P.; Anwar, M. M.; Kitteringham, N.; Park, B. K.; Souma, T.; Moriguchi, T.; Yamamoto, M. Transcriptional Control of Glyoxalase 1 by Nrf2 Provides a Stress-Responsive Defence against Dicarbonyl Glycation. *Biochem. J.* **2012**, *443* (1), 213–222.
(41) Urscher, M.; Alisch, R.; Deponte, M. The Glyoxalase System of Malaria Parasites—Implications for Cell Biology and General Glyoxalase Research. In *Seminars in Cell & Developmental Biology*; Elsevier, 2011; Vol. 22, pp 262–270.
(42) Antognelli, C.; Ferri, I.; Bellezza, G.; Siccu, P.; Love, H. D.; Talesa, V. N.; Sidoni, A. Glyoxalase 2 Drives Tumorigenesis in Human Prostate Cells in a Mechanism Involving Androgen Receptor and P53-p21 Axis. *Mol. Carcinog.* **2017**, *56* (9), 2112–2126.
(43) Crowder, M. W.; Maiti, M. K.; Banovic, L.; Makaroff, C. A. Glyoxalase II from A. Thaliana Requires Zn (II) for Catalytic Activity. *Febs Lett.* **1997**, *418* (3), 351–354.
(44) Limphong, P.; McKinney, R. M.; Adams, N. E.; Bennett, B.; Makaroff, C. A.; Gunasekera, T.; Crowder, M. W. Human Glyoxalase II Contains an Fe (II) Zn (II) Center but Is Active as a Mononuclear Zn (II) Enzyme. *Biochemistry* **2009**, *48* (23), 5426–5434.
(45) Beveridge, D. L.; Dicapua, F. M. Free-Energy Via Molecular Simulation - Applications to Chemical and Biomolecular Systems. *Annu. Rev. Biophys. Biomol. Struct.* **1989**, *18*, 431.
(46) Campos-Bermudez, V. A.; Leite, N. R.; Krog, R.; Costa-Filho, A. J.; Soncini, F. C.; Oliva, G.; Vila, A. J. Biochemical and Structural Characterization of Salmonella Typhimurium Glyoxalase II: New Insights into Metal Ion Selectivity. *Biochemistry* **2007**, *46* (39), 11069–11079.
(47) Kondoh, Y.; Kawase, M.; Hirata, M.; Ohmori, S. Carbon Sources for D-Lactate Formation in Rat Liver. *J. Biochem.* **1994**, *115* (3), 590–595.
(48) Chen, S.-L.; Fang, W.-H.; Himo, F. Theoretical Study of the Phosphotriesterase Reaction Mechanism. *J. Phys. Chem. B* **2007**, *111* (6), 1253–1255.
(49) Wong, K.-Y.; Gao, J. The Reaction Mechanism of Paraoxon Hydrolysis by Phosphotriesterase from Combined QM/MM Simulations. *Biochemistry* **2007**, *46* (46), 13352–13369.
(50) Liao, R. Z.; Yu, J. G.; Himo, F. Reaction Mechanism of the Dinuclear Zinc Enzyme N-Acyl-L-Homoserine Lactone Hydrolase: A Quantum Chemical Study. *Inorg. Chem.* **2009**, *48* (4), 1442–1448. https://doi.org/10.1021/IC801531N.
(51) Liao, R.-Z.; Himo, F.; Yu, J.-G.; Liu, R.-Z. Dipeptide Hydrolysis by the Dinuclear Zinc Enzyme Human Renal Dipeptidase: Mechanistic Insights from DFT Calculations. *J. Inorg. Biochem.* **2010**, *104* (1), 37–46.
(52) Bím, D.; Navrátil, M.; Gutten, O.; Konvalinka, J.; Kutil, Z.; Culka, M.; Navrátil, V.; Alexandrova, A. N.; Bařinka, C.; Rulíšek, L. Predicting Effects of Site-Directed Mutagenesis on Enzyme Kinetics by QM/MM and QM Calculations: A Case of Glutamate Carboxypeptidase II. *J. Phys. Chem. B* **2022**, *126* (1), 132–143.
(53) Park, H.; Brothers, E. N.; Merz, K. M. Hybrid QM/MM and DFT Investigations of the Catalytic Mechanism and Inhibition of the Dinuclear Zinc Metallo-β-Lactamase CcrA from Bacteroides Fragilis. *J. Am. Chem. Soc.* **2005**, *127* (12), 4232–4241.
(54) Medina, F. E.; Jaña, G. A. QM/MM Study of a VIM-1 Metallo-β-Lactamase Enzyme: The Catalytic Reaction Mechanism. *ACS Catal.* **2021**, *12* (1), 36–47.
(55) Zang, T. M.; Hollman, D. A.; Crawford, P. A.; Crowder, M. W.; Makaroff, C. A. Arabidopsis Glyoxalase II Contains a Zinc/Iron Binuclear Metal Center That Is Essential for Substrate Binding and Catalysis* 210. *J. Biol. Chem.* **2001**, *276* (7), 4788–4795.
(56) Chen, S.-L.; Fang, W.-H.; Himo, F. Reaction Mechanism of the Binuclear Zinc Enzyme

Glyoxalase II–A Theoretical Study. *J. Inorg. Biochem.* **2009**, *103* (2), 274–281.
(57) Jafari, S.; Ryde, U.; Fouda, A. E. A.; Alavi, F. S.; Dong, G.; Irani, M. Quantum Mechanics/Molecular Mechanics Study of the Reaction Mechanism of Glyoxalase I. *Inorg. Chem.* **2020**, *59* (4), 2594–2603. https://doi.org/10.1021/acs.inorgchem.9b03621.
(58) Jafari, S.; Ryde, U.; Irani, M. QM/MM Study of the Stereospecific Proton Exchange of Glutathiohydroxyacetone by Glyoxalase I. *Results Chem.* **2019**, *1*, 100011.
(59) Jafari, S.; Ryde, U.; Irani, M. Two-Substrate Glyoxalase I Mechanism; a Quantum Mechanics/Molecular Mechanics Study. *Inorg. Chem.* **2020**, https://doi.org/10.1021/acs.inorgchem.0c02957.
(60) Bas, D. C.; Rogers, D. M.; Jensen, J. H. Very Fast Prediction and Rationalization of PKa Values for Protein–Ligand Complexes. *Proteins Struct. Funct. Bioinforma.* **2008**, *73* (3), 765–783.
(61) Olsson, M. H. M.; Søndergaard, C. R.; Rostkowski, M.; Jensen, J. H. PROPKA3: Consistent Treatment of Internal and Surface Residues in Empirical PKa Predictions. *J. Chem. Theory Comput.* **2011**, *7* (2), 525–537. https://doi.org/10.1021/ct100578z.
(62) Jensen, J. H.; Li, H.; Robertson, A. D.; Molina, P. A. Prediction and Rationalization of Protein p K a Values Using QM and QM/MM Methods. *J. Phys. Chem. A* **2005**, *109* (30), 6634–6643.
(63) Le Grand, S.; Götz, A. W.; Walker, R. C. SPFP: Speed without Compromise - A Mixed Precision Model for GPU Accelerated Molecular Dynamics Simulations. *Comput. Phys. Commun.* **2013**, *184* (2), 374–380. https://doi.org/10.1016/j.cpc.2012.09.022.
(64) Salomon-Ferrer, R.; Götz, A. W.; Poole, D.; Le Grand, S.; Walker, R. C. Routine Microsecond Molecular Dynamics Simulations with AMBER on GPUs. 2. Explicit Solvent Particle Mesh Ewald. *J. Chem. Theory Comput.* **2013**, *9* (9), 3878–3888. https://doi.org/10.1021/ct400314y.
(65) Götz, A. W.; Williamson, M. J.; Xu, D.; Poole, D.; Le Grand, S.; Walker, R. C. Routine Microsecond Molecular Dynamics Simulations with AMBER on GPUs. 1. Generalized Born. *J. Chem. Theory Comput.* **2012**, *8* (5), 1542–1555. https://doi.org/10.1021/ct200909j.
(66) Case, D. A.; Ben-Shalom, I. Y.; Brozell, S. R.; Cerutti, D. S.; Cheatham, T. E.; III; Cruzeiro, V. W. D.; Darden, T. A.; Duke, R. E.; Ghoreishi, D.; Gilson, M. K.; Gohlke, H.; Goetz, A. W.; Greene, D.; Harris, R.; Homeyer, N.; Izadi, S.; Kovalenko, A.; Kurtzman, T.; Lee, T. S.; LeGrand, S.; Li, P.; Lin, C.; Liu, J.; Luchko, T.; Luo, R.; Mermelstein, D. J.; Merz, K. M.; Miao, Y.; Monard, G.; Nguyen, C.; Nguyen, H.; Omelyan, I.; Onufriev, A.; Pan, F.; Qi, R.; Roe, D. R.; Roitberg, A.; Sagui, C.; Schott-Verdugo, S.; Shen, J.; Simmerling, C. L.; Smith, J.; Salomon-Ferrer, R.; Swails, J.; Walker, R. C.; Wang, J.; Wei, H.; Wolf, R. M.; Wu, X.; Xiao, L.; York, D. M.; Kollman, P. A. Amber 20, University of California, San Francisco. 2020.
(67) Maier, J. A.; Martinez, C.; Kasavajhala, K.; Wickstrom, L.; Hauser, K. E.; Simmerling, C. Ff14SB: Improving the Accuracy of Protein Side Chain and Backbone Parameters from Ff99SB. *J. Chem. Theory Comput.* **2015**, *11* (8), 3696–3713. https://doi.org/10.1021/acs.jctc.5b00255.
(68) Wang, J.; Wolf, R. M.; Caldwell, J. W.; Kollman, P. A.; Case, D. A. Development and Testing of a General Amber Force Field. *J. Comput. Chem.* **2004**, *25* (9), 1157–1174. https://doi.org/10.1002/jcc.20035.
(69) Lee, C.; Yang, W.; Parr, G, R. Development of the Colic-Salvetti Correlation-Energy into a Functional of the Electron Density. *Am. Phys. Soc.* **1988**, *37* (2), 785–789.
(70) Becke, A. D. Density-Functional Exchange-Energy Approximation with Correct Asymptotic Behavior. *Phys. Rev. A* **1988**, *38* (6), 3098–3100.
(71) Becke, A. D. Density-Functional Thermochemistry. III. The Role of Exact Exchange. *J. Chem. Phys.* **1993**, *98*, 5648–5652. https://doi.org/10.1063/1.464913.
(72) Petersson, G. A.; Al-Laham, M. A. A Complete Basis Set Model Chemistry. II. Open-shell Systems and the Total Energies of the First-row Atoms. *J. Chem. Phys.* **1991**, *94* (9), 6081–6090. https://doi.org/10.1063/1.460447.
(73) Petersson, G. A.; Bennett, A.; Tensfeldt, T. G.; Al-Laham, M. A.; Shirley, W. A.; Mantzaris, J. A Complete Basis Set Model Chemistry. I. The Total Energies of Closed-Shell Atoms and Hydrides of the First-Row Elements. *J. Chem. Phys.* **1988**, *89* (4), 2193–2218. https://doi.org/10.1063/1.455064.

(74) Besler, B. H.; Merz, K. M.; Kollman, P. A. Atomic Charges Derived from Semiempirical Methods. *J. Comput. Chem.* **1990**, *11* (4), 431–439. https://doi.org/10.1002/jcc.540110404.
(75) Frisch, M. J.; Trucks, G. W.; Schlegel, H. B.; Scuseria, G. E.; Robb, M. A.; Cheeseman, J. R.; Scalmani, G.; Barone, V.; Petersson, G. A.; Nakatsuji, H.; Li, X.; Caricato, M.; Marenich, A. V; Bloino, J.; Janesko, B. G.; Gomperts, R.; Mennucci, B.; Hratchian, H. P.; Ortiz, J. V; Izmaylov, A. F.; Sonnenberg, J. L.; Williams; Ding, F.; Lipparini, F.; Egidi, F.; Goings, J.; Peng, B.; Petrone, A.; Henderson, T.; Ranasinghe, D.; Zakrzewski, V. G.; Gao, J.; Rega, N.; Zheng, G.; Liang, W.; Hada, M.; Ehara, M.; Toyota, K.; Fukuda, R.; Hasegawa, J.; Ishida, M.; Nakajima, T.; Honda, Y.; Kitao, O.; Nakai, H.; Vreven, T.; Throssell, K.; Montgomery Jr., J. A.; Peralta, J. E.; Ogliaro, F.; Bearpark, M. J.; Heyd, J. J.; Brothers, E. N.; Kudin, K. N.; Staroverov, V. N.; Keith, T. A.; Kobayashi, R.; Normand, J.; Raghavachari, K.; Rendell, A. P.; Burant, J. C.; Iyengar, S. S.; Tomasi, J.; Cossi, M.; Millam, J. M.; Klene, M.; Adamo, C.; Cammi, R.; Ochterski, J. W.; Martin, R. L.; Morokuma, K.; Farkas, O.; Foresman, J. B.; Fox, D. J. Gaussian 16. Wallingford, CT 2016.
(76) Bayly, C. I.; Cieplak, P.; Cornell, W.; Kollman, P. A. A Well-Behaved Electrostatic Potential Based Method Using Charge Restraints for Deriving Atomic Charges: The RESP Model. *J. Phys. Chem.* **1993**, *97* (40), 10269–10280. https://doi.org/10.1021/j100142a004.
(77) Hu, L.; Ryde, U. Comparison of Methods to Obtain Force-Field Parameters for Metal Sites. *J. Chem. Theory Comput.* **2011**, *7* (8), 2452–2463. https://doi.org/10.1021/ct100725a.
(78) Schäfer, A.; Horn, H.; Ahlrichs, R. Fully Optimized Contracted Gaussian-Basis Sets for Atoms Li to Kr. *J. Chem. Phys.* **1992**, *97* (4), 2571–2577. https://doi.org/10.1063/1.463096.
(79) Tao, J.; Perdew, J. P.; Staroverov, V. N.; Scuseria, G. E. Climbing the Density Functional Ladder: Nonempirical Meta–Generalized Gradient Approximation Designed for Molecules and Solids. *Phys. Rev. Lett.* **2003**, *91* (14), 146401. https://doi.org/10.1103/PhysRevLett.91.146401.
(80) Furche, F.; Ahlrichs, R.; Hättig, C.; Klopper, W.; Sierka, M.; Weigend, F. Turbomole. *Wiley Interdiscip. Rev. Comput. Mol. Sci.* **2014**, *4* (2), 91–100. https://doi.org/10.1002/wcms.1162.
(81) Eichkorn, K.; Treutler, O.; Öhm, H.; Häser, M.; Ahlrichs, R. Auxiliary Basis Sets to Approximate Coulomb Potentials. *Chem. Phys. Lett.* **1995**, *240*, 283–290. https://doi.org/https://doi.org/10.1016/0009-2614(95)00621-A.
(82) Eichkorn, K.; Weigend, F.; Treutler, O.; Ahlrichs, R. Auxiliary Basis Sets for Main Row Atoms and Transition Metals and Their Use to Approximate Coulomb Potentials. *Theor. Chem. Accounts Theory, Comput. Model. (Theoretica Chim. Acta)* **1997**, *97* (1–4), 119–124. https://doi.org/10.1007/s002140050244.
(83) Grimme, S.; Antony, J.; Ehrlich, S.; Krieg, H. A Consistent and Accurate Ab Initio Parametrization of Density Functional Dispersion Correction (DFT-D) for the 94 Elements H-Pu. *J. Chem. Phys.* **2010**, *132* (15), 154104. https://doi.org/10.1063/1.3382344.
(84) Grimme, S.; Ehrlich, S.; Goerigk, L. Effect of the Damping Function in Dispersion Corrected Density Functional Theory. *J. Comput. Chem.* **2011**, *32* (7), 1456–1465. https://doi.org/10.1002/jcc.21759.
(85) Seminario, J. M. Calculation of Intramolecular Force Fields from Second-Derivative Tensors. *Int. J. Quantum Chem.* **1996**, *60* (7), 1271–1277. https://doi.org/10.1002/(SICI)1097-461X(1996)60:7<1271::AID-QUA8>3.0.CO;2-W.
(86) Nilsson, K.; Lecerof, D.; Sigfridsson, E.; Ryde, U. An Automatic Method to Generate Force-Field Parameters for Hetero-Compounds. *Acta Crystallogr. - Sect. D Biol. Crystallogr.* **2003**, *59* (2), 274–289. https://doi.org/10.1107/S0907444902021431.
(87) Jafari, S.; Kazemi, N.; Ryde, U.; Irani, M. Higher Flexibility of Glu-172 Explains the Unusual Stereospecificity of Glyoxalase I. *Inorg. Chem.* **2018**, *57*, 4944–4958. https://doi.org/10.1021/acs.inorgchem.7b03215.
(88) Jorgensen, W. L.; Chandrasekhar, J.; Madura, J. D.; Impey, R. W.; Klein, M. L. Comparison of Simple Potential Functions for Simulating Liquid Water. *J. Chem. Phys.* **1983**, *79* (2), 926–935. https://doi.org/10.1063/1.445869.
(89) Joung, I. S.; Cheatham, T. E. Determination of Alkali and Halide Monovalent Ion Parameters for Use in Explicitly Solvated Biomolecular Simulations. *J. Phys. Chem. B* **2008**, *112* (30),

9020–9041. https://doi.org/10.1021/JP8001614/SUPPL_FILE/JP8001614-FILE003.PDF.
(90) Roe, D. R.; Cheatham, T. E. PTRAJ and CPPTRAJ: Software for Processing and Analysis of Molecular Dynamics Trajectory Data. *J. Chem. Theory Comput.* **2013**, *9* (7), 3084–3095. https://doi.org/10.1021/ct400341p.
(91) Case, D. A.; Cheatham, T. E.; Darden, T.; Gohlke, H.; Luo, R.; Merz, K. M.; Onufriev, A.; Simmerling, C.; Wang, B.; Woods, R. J. The Amber Biomolecular Simulation Programs. *Journal of Computational Chemistry*. Wiley Subscription Services, Inc., A Wiley Company December 2005, pp 1668–1688. https://doi.org/10.1002/jcc.20290.
(92) Ryckaert, J. P.; Ciccotti, G.; Berendsen, H. J. . Numerical Integration of the Cartesian Equations of Motion of a System with Constraints: Molecular Dynamics of n-Alkanes. *J. Comput. Phys.* **1977**, *23* (3), 327–341. https://doi.org/10.1016/0021-9991(77)90098-5.
(93) Wu, X.; Brooks, B. R. Self-Guided Langevin Dynamics Simulation Method. *Chem. Phys. Lett.* **2003**, *381* (3–4), 512–518. https://doi.org/10.1016/j.cplett.2003.10.013.
(94) Berendsen, H. J. C.; Postma, J. P. M.; van Gunsteren, W. F.; DiNola, A.; Haak, J. R. Molecular Dynamics with Coupling to an External Bath. *J. Chem. Phys.* **1984**, *81* (8), 3684–3690. https://doi.org/10.1063/1.448118.
(95) Darden, T.; York, D.; Pedersen, L. Particle Mesh Ewald: An N·log(N) Method for Ewald Sums in Large Systems. *J. Chem. Phys.* **1993**, *98* (12), 10089–10092. https://doi.org/10.1063/1.464397.
(96) Ryde, U. QM/MM Calculations on Proteins. *Methods Enzymol.* **2016**, *577*, 119–158. https://doi.org/10.1016/BS.MIE.2016.05.014.
(97) Senn, H. M.; Thiel, W. QM/MM Methods for Biomolecular Systems. *Angew. Chemie - Int. Ed.* **2009**, *48* (7), 1198–1229. https://doi.org/10.1002/anie.200802019.
(98) Ryde, U. The Coordination of the Catalytic Zinc in Alcohol Dehydrogenase Studied by Combined Quantum-Chemical and Molecular Mechanics Calculations. *J. Comput. Aided. Mol. Des.* **1996**, *10* (2), 153–164. https://doi.org/10.1007/BF00402823.
(99) Ryde, U.; Olsson, M. H. M. Structure, Strain, and Reorganization Energy of Blue Copper Models in the Protein. *Int. J. Quantum Chem.* **2001**, *81* (5), 335–347.
(100) Von Arnim, M.; Ahlrichs, R. Performance of Parallel TURBOMOLE for Density Functional Calculations. *J. Comput. Chem.* **1998**, *19* (15), 1746–1757. https://doi.org/10.1002/(SICI)1096-987X(19981130)19:15<1746::AID-JCC7>3.0.CO;2-N.
(101) Case, D. A.; Babin, V.; Berryman, J. T.; Betz, R. M.; Cai, Q.; Cerutti, D. S.; Cheatham, T. E.; Darden, T. A.; Duke, R. E.; Gohlke, H.; Goetz, A. W.; Gusarov, S.; Homeyer, N.; Janowski, P.; Kaus, J.; Kolossváry, I.; Kovalenko, A.; Lee, T. S.; LeGrand, S.; Luchko, T.; Luo, R.; Madej, B.; Merz, K. M.; Paesani, F.; Roe, D. R.; Roitberg, A.; Sagui, C.; Salomon-Ferrer, R.; Seabra, G.; Simmerling, C. L.; Smith, W.; Swails, J.; Walker; Wang, J.; Wolf, R. M.; Wu, X.; Kollman, P. A. Amber 14, University of California: San Francisco, 2014.
(102) Reuter, N.; Dejaegere, A.; Maigret, B.; Karplus, M. Frontier Bonds in QM/MM Methods: A Comparison of Different Approaches. *J. Phys. Chem. A* **2000**, *104* (8), 1720–1735. https://doi.org/10.1021/jp9924124.
(103) Hu, L.; Söderhjelm, P.; Ryde, U. On the Convergence of QM/MM Energies. *J. Chem. Theory Comput.* **2011**, *7* (3), 761–777. https://doi.org/10.1021/ct100530r.
(104) Svensson, M.; Humbel, S.; Froese, R. D. J.; Matsubara, T.; Sieber, S.; Morokuma, K. ONIOM: A Multilayered Integrated MO + MM Method for Geometry Optimizations and Single Point Energy Predictions. A Test for Diels−Alder Reactions and Pt(P(t -Bu) 3) 2 + H 2 Oxidative Addition. *J. Phys. Chem.* **2002**, *100* (50), 19357–19363. https://doi.org/10.1021/jp962071j.
(105) Cao, L.; Ryde, U. On the Difference between Additive and Subtractive QM/MM Calculations. *Front. Chem.* **2018**, *6*, 89.
(106) Hu, L.; Eliasson, J.; Heimdal, J.; Ryde, U. Do Quantum Mechanical Energies Calculated for Small Models of Protein-Active Sites Converge? *J. Phys. Chem. A* **2009**, *113* (43), 11793–11800. https://doi.org/10.1021/jp9029024.
(107) Sumner, S.; Söderhjelm, P.; Ryde, U. Effect of Geometry Optimizations on QM-Cluster and QM/MM Studies of Reaction Energies in Proteins. *J. Chem. Theory Comput.* **2013**, *9* (9), 4205–

4214. https://doi.org/10.1021/ct400339c.
(108) Hu, L.; Söderhjelm, P.; Ryde, U. Accurate Reaction Energies in Proteins Obtained by Combining QM/MM and Large QM Calculations. *J. Chem. Theory Comput.* **2013**, *9* (1), 640–649. https://doi.org/10.1021/ct3005003.
(109) Sierka, M.; Hogekamp, A.; Ahlrichs, R. Fast Evaluation of the Coulomb Potential for Electron Densities Using Multipole Accelerated Resolution of Identity Approximation. *J. Chem. Phys.* **2003**, *118* (20), 9136–9148. https://doi.org/10.1063/1.1567253.
(110) Weigend, F.; Ahlrichs, R. Balanced Basis Sets of Split Valence, Triple Zeta Valence and Quadruple Zeta Valence Quality for H to Rn: Design and Assessment of Accuracy. *Phys. Chem. Chem. Phys.* **2005**, *7* (18), 3297. https://doi.org/10.1039/b508541a.
(111) Rappoport, D.; Furche, F. Property-Optimized Gaussian Basis Sets for Molecular Response Calculations. *J. Chem. Phys.* **2010**, *133* (13), 134105.
(112) Kaukonen, M.; Söderhjelm, P.; Heimdal, J.; Ryde, U. Proton Transfer at Metal Sites in Proteins Studied by Quantum Mechanical Free-Energy Perturbations. *J. Chem. Theory Comput.* **2008**, *4* (6), 985–1001. https://doi.org/10.1021/ct700347h.
(113) Luzhkov, V.; Warshel, A. Microscopic Models for Quantum Mechanical Calculations of Chemical Processes in Solutions: LD/AMPAC and SCAAS/AMPAC Calculations of Solvation Energies. *J. Comput. Chem.* **1992**, *13* (2), 199–213. https://doi.org/10.1002/jcc.540130212.
(114) Rod, T. H.; Ryde, U. Quantum Mechanical Free Energy Barrier for an Enzymatic Reaction. *Phys. Rev. Lett.* **2005**, *94*, 138302. https://doi.org/10.1103/PhysRevLett.94.138302.
(115) Rod, T. H.; Ryde, U. Accurate QM/MM Free Energy Calculations of Enzyme Reactions: Methylation by Catechol O-Methyltransferase. *J. Chem. Theory Comput.* **2005**, *1*, 1240–1251. https://doi.org/10.1021/ct0501102.
(116) Heimdal, J.; Kaukonen, M.; Srnec, M.; Rulíšek, L.; Ryde, U. Reduction Potentials and Acidity Constants of Mn Superoxide Dismutase Calculated by QM/MM Free-Energy Methods. *ChemPhysChem* **2011**, *12* (17), 3337–3347. https://doi.org/10.1002/cphc.201100339.
(117) Guha, M. K.; Vander Jagt, D. L.; Creighton, D. J. Diffusion-Dependent Rates for the Hydrolysis Reaction Catalyzed by Glyoxalase II from Rat Erythrocytes. *Biochemistry* **1988**, *27* (24), 8818–8822.
(118) Jafari, S.; Ryde, U.; Irani, M. QM/MM Study of the Catalytic Reaction of Myrosinase; Importance of Assigning Proper Protonation States of Active-Site Residues. *J. Chem. Theory Comput.* **2021**, *17* (3), 1822–1841. https://doi.org/10.1021/acs.jctc.0c01121.
(119) Uranga, J.; Mikulskis, P.; Genheden, S.; Ryde, U. Can the Protonation State of Histidine Residues Be Determined from Molecular Dynamics Simulations? *Comput. Theor. Chem.* **2012**, *1000*, 75–84. https://doi.org/10.1016/j.comptc.2012.09.025.
(120) Cao, L.; Caldararu, O.; Ryde, U. Protonation States of Homocitrate and Nearby Residues in Nitrogenase Studied by Computational Methods and Quantum Refinement. *J. Phys. Chem. B* **2017**, *121*, 8242–8262. https://doi.org/10.1021/acs.jpcb.7b02714.
(121) Pettersen, E. F.; Goddard, T. D.; Huang, C. C.; Couch, G. S.; Greenblatt, D. M.; Meng, E. C.; Ferrin, T. E. UCSF Chimera—a Visualization System for Exploratory Research and Analysis. *J. Comput. Chem.* **2004**, *25* (13), 1605–1612.
(122) Dal Peraro, M.; Vila, A. J.; Carloni, P. Protonation State of Asp120 in the Binuclear Active Site of the Metallo-β-Lactamase from Bacteroides Fragilis. *Inorg. Chem.* **2003**, *42* (14), 4245–4247.

TOC Graphic

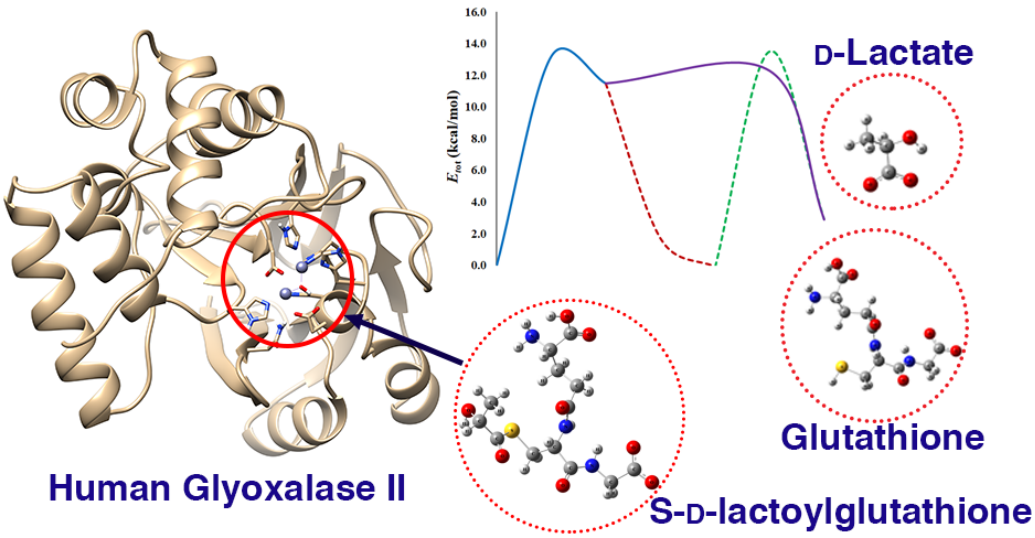

The catalytic reaction of human Glyoxalase II was investigated using a Quantum Mechanics/Molecular Mechanics (QM/MM) model. A new mechanism was proposed for this enzyme. It was demonstrated that assigning correct protonation states of active site residues is a key factor for investigating enzymatic reaction mechanisms.